

<https://doi.org/10.1038/s43247-025-02424-9>

# Nanoscale chemical heterogeneities control the viscosity of andesitic magmas

Check for updates

Pedro Valdivia<sup>1,2</sup>✉, Alessio Zandonà<sup>3</sup>, Jessica Löschmann<sup>3</sup>, Dmitry Bondar<sup>1,2</sup>, Cécile Genevois<sup>4</sup>, Aurélien Canizarès<sup>4</sup>, Mathieu Allix<sup>4</sup>, Nobuyoshi Miyajima<sup>1</sup>, Alexander Kurnosov<sup>1</sup>, Tiziana Boffa Ballaran<sup>1</sup>, Fabrizio Di Fiore<sup>5</sup>, Alessandro Vona<sup>6</sup>, Claudia Romano<sup>6</sup>, Joachim Deubener<sup>3</sup>, Emily C. Bamber<sup>2,7</sup>, Alessandro Longo<sup>8</sup> & Danilo Di Genova<sup>2</sup>

Explosive volcanic eruptions, driven by magma fragmentation, pose significant geohazards due to their rapid energy release and widespread dispersal of pyroclasts. High magma viscosity promotes brittle fragmentation by limiting volatile escape and enhancing internal pressure buildup. Although recent studies have recognized that iron-titanium oxide nanocrystal formation increases melt viscosity, the mechanisms underlying this effect remain poorly constrained. Here we quantify the influence of nanocrystallization on magma viscosity by developing viscosity models that incorporate iron-titanium variations, calibrated against nanocrystal-free andesitic melts. Using time-resolved imaging, we show that nanocrystals form within seconds within synthetic andesitic melts. This process generates nanoscale chemical heterogeneities, including silica enrichment in the surrounding melt and aluminum-rich shells embedding the nanocrystals. These heterogeneities result in viscosity increases of up to 30-fold at eruptive temperatures. Our findings indicate that nanocrystallization modulates magma rheology during early crystallization, with direct implications for the dynamics of andesitic eruptions.

Explosive eruptions are recognized as one of the most hazardous natural phenomena on Earth<sup>1</sup>, capable of injecting a large amount of gas and ash into the atmosphere, posing a threat to inhabited regions. These eruptions stem from magma fragmentation, the process by which a hot gas-pyroclast mixture is produced<sup>2–5</sup>. The triggers of magma fragmentation are twofold: bubble overpressure caused by limited bubble growth due to high viscosity<sup>6,7</sup>, and strain rates that exceed the relaxation time of the melt, which is controlled by its chemical composition<sup>2,8,9</sup>. Moreover, disequilibrium crystallization and degassing during magma ascent contribute to the enhanced explosivity of volcanic eruptions<sup>10–13</sup> by increasing melt viscosity<sup>14,15</sup>, which hinders gas bubble expansion<sup>16</sup>. Several studies<sup>10,11,17,18</sup> have shown that the syn-eruptive disequilibrium crystallization of microlites increases magma viscosity, generating overpressure that can lead to explosive eruptions<sup>3–5</sup>.

Previous authors<sup>19–23</sup> have shown that the formation of Fe-Ti-oxide nanocrystals (nanolites) increases the viscosity of volcanic melts in

laboratory measurements. Given that nanolites are commonly found in volcanic products from explosive events<sup>24–32</sup>, this supports the hypothesis that they influence magma ascent dynamics and eruptive style. Several mechanisms have been proposed: nanolite-induced chemical changes that increase magma viscosity<sup>19,33,34</sup>, solid aggregation that hinders melt flow<sup>35</sup>, and enhanced heterogeneous bubble nucleation that affects degassing<sup>36</sup>. Recent work<sup>29,32,37</sup> suggests that nanolites can serve as indicators of the physicochemical conditions of magma during transitions in eruptive style at andesitic volcanoes, also contributing to the rheological changes that promote more explosive behavior. However, despite accumulating evidence for their presence in explosive volcanic products, the extent and mechanisms of how nanolites influence magma rheology remain poorly constrained<sup>19,20,27,29,32,33,35–38</sup>.

To the best of our knowledge, this study reports the first in situ, high-temperature imaging observation of nanolite formation in a synthetic andesitic melt. We leverage these observations to investigate the connection

<sup>1</sup>Bayerisches Geoinstitut, University of Bayreuth, Universitätsstraße 30, 95447 Bayreuth, Germany. <sup>2</sup>Institute of Science, Technology and Sustainability for Ceramics (ISSMC) of the National Research Council (CNR), Via Granarolo 64, I-48018 Faenza, RA, Italy. <sup>3</sup>Institute of Non-Metallic Materials, Clausthal University of Technology, Zehntnerstraße 2a, D-38678 Clausthal-Zellerfeld, Germany. <sup>4</sup>CNRS, CEMHTI UPR3079, Univ, Orléans, France. <sup>5</sup>Istituto Nazionale di Geofisica e Vulcanologia, Sezione Roma 1, Via di Vigna Murata 605, 00143 Rome, Italy. <sup>6</sup>Dipartimento di Scienze, Università degli Studi Roma Tre, Largo San L. Murialdo 1, 00146 Rome, Italy. <sup>7</sup>Department of Earth Sciences, University of Turin, Via Valperga Caluso, 35, 10125 Turin, Italy. <sup>8</sup>ESRF - The European Synchrotron, 38043 Grenoble, France. ✉e-mail: [pedro.valdivia-munoz@uni-bayreuth.de](mailto:pedro.valdivia-munoz@uni-bayreuth.de)

between nanolite formation and the flow properties of various andesitic compositions. To establish a reliable basis for comparison, we develop chemical-dependent viscosity models using only viscosity data derived from samples free of nanolites. This approach is necessary because previous studies, including widely used viscosity models<sup>39</sup>, tend to overestimate the viscosity of melts prone to nanocrystallization<sup>20,21,25,40</sup>. Our results show that nanolite formation induces nanoscale chemical variations in the melt. These nanodomains increase melt viscosity and can significantly alter the physical properties of magma. This suggests that nanoscale chemical thresholds may influence magma properties and dynamics at early stages of crystallization.

## Results and discussion

### Preliminary in situ observations of nanolite formation during heating

We produced four anhydrous andesitic melts and one transition-metal-free analogue (Table 1). The sample AND100 ( $\text{Fe}^{3+}/\text{Fe}_{\text{tot}} = 0.64$ ) was designed to mirror the andesitic chemical composition of the magma erupted at Sakurajima volcano described in Okumura et al.<sup>19</sup>. Samples AND100red ( $\text{Fe}^{3+}/\text{Fe}_{\text{tot}} = 0.27$ ) and AND100ox ( $\text{Fe}^{3+}/\text{Fe}_{\text{tot}} = 0.71$ ) represent isochemical analogues of AND100 with lower and higher  $\text{Fe}^{3+}/\text{Fe}_{\text{tot}}$ , respectively (Table 1). AND65 ( $\text{Fe}^{3+}/\text{Fe}_{\text{tot}} = 0.74$ ) and AND0 were produced based on the composition of AND100, from which 35% and 100% of the total transition metal content ( $\text{FeO}_{\text{tot}}$ ,  $\text{TiO}_2$  and  $\text{MnO}$ ) were removed. The amorphous nature of all samples was confirmed through a combination of scanning electron microscopy (SEM) imaging in backscattered electron (BSE) mode and Raman spectroscopy analysis; additional details can be found in the Supplementary Information (Supplementary Preliminary Characterization; Supplementary Fig. 1).

We initially explored the nanoscale textural response of the AND100 composition from a fundamental standpoint, performing in situ high-temperature measurements. High-temperature Raman results<sup>41</sup> (Fig. 1a) reveal that the amorphous state of AND100 is considerably unstable against thermal treatments, leading to the formation of nano-sized titanomagnetite crystals already  $\sim 70$  °C above the glass transition temperature ( $T_g$ ), which was determined by conventional differential scanning calorimetry (C-DSC) (Table 1, Supplementary Table 2). This is evidenced by the appearance of vibrational features that can be assigned to Fe-Ti-oxides such as

titanomagnetite<sup>40–44</sup>, which become even more distinctive upon cooling the samples to room temperature (Supplementary Fig. 4b; Supplementary Post-in situ Raman). To monitor the nanoscale changes associated with the non-stoichiometric precipitation of titanomagnetite, we also performed in situ nanoscale observation of nanolite formation in an andesitic composition using transmission electron microscopy (TEM) combined with a heating stage (Supplementary Movie). The experimental procedure, as previously optimized by Zandonà et al.<sup>45</sup>, minimized possible artifacts arising from electron irradiation, which could be limited to a simple shift of thermally activated processes (i.e., phase separation and crystallization) to lower temperatures and a minor loss of alkalis during the heating in vacuum. During the heating experiment (Fig. 1b), we observed that the starting material, which appeared homogeneous within the experimental resolution, rapidly underwent amorphous phase separation<sup>46</sup>, possibly due to liquid-liquid immiscibility<sup>47</sup> or simply corresponding to a kinetically favored metastable stage of chemical clustering preceding non-isochemical crystal nucleation in the melt. This process led to the development of sub-rounded ( $<5$  nm in diameter) higher-contrast domains that lacked crystalline order, as initially determined by local Fast Fourier transforms (FFTs) of the collected TEM images (Fig. 1b). Notably, these chemically differentiated nanodomains exhibited structural ordering into iron-rich nanosized crystals at higher temperatures ( $>550$  °C), followed by gradual growth and accompanied by the development of aluminum-rich domains (Supplementary Fig. 5). Fast Fourier transforms (FFTs) of images acquired at this stage (Fig. 1b) are consistent with the formation of titanomagnetite<sup>48,49</sup>. Energy-dispersive X-ray spectra (EDS) acquired before and after the in situ experiment (Supplementary Table 3) confirmed that the overall bulk composition remained almost constant after the experiment, except for an unavoidable loss of alkalis due to electron irradiation in a vacuum. The observed mechanism, i.e., amorphous phase separation, followed by the rapid formation and growth of nanocrystals within Fe-enriched domains, has previously been reported for other aluminosilicate glasses and melts<sup>21,50</sup> and also mirrors those inferred from ex-situ observations on basaltic and basanitic melts<sup>21,51</sup>. Therefore, they provide an accurate overview of the nanocrystallization processes that should be expected to occur in deeply supercooled melts and reheated glasses of andesitic composition.

**Table 1 | Chemical analysis results<sup>a</sup> (wt%) and parameters used for melt viscosity parameterization using the MYEGA equation (Eq. 5)**

	AND100	AND100red	AND100ox	AND65	AND0
$\text{SiO}_2$	60.38 (0.36)	60.47 (0.40)	60.56 (0.35)	62.52 (0.19)	65.91 (0.34)
$\text{TiO}_2$	0.79 (0.04)	0.80 (0.07)	0.81 (0.06)	0.56 (0.04)	0.04 (0.03)
$\text{Al}_2\text{O}_3$	16.69 (0.18)	16.83 (0.22)	16.79 (0.19)	17.28 (0.22)	18.01 (0.11)
$\text{FeO}_{\text{tot}}$	6.77 (0.12)	6.87 (0.12)	6.76 (0.15)	4.40 (0.11)	0.04 (0.03)
$\text{MnO}$	0.17 (0.03)	0.18 (0.04)	0.18 (0.03)	0.11 (0.03)	0.01 (0.01)
$\text{MgO}$	3.00 (0.07)	2.94 (0.06)	2.95 (0.06)	3.02 (0.07)	3.21 (0.06)
$\text{CaO}$	6.62 (0.09)	6.51 (0.11)	6.49 (0.11)	6.76 (0.13)	7.26 (0.11)
$\text{Na}_2\text{O}$	3.50 (0.15)	3.46 (0.10)	3.40 (0.10)	3.49 (0.11)	3.82 (0.14)
$\text{K}_2\text{O}$	1.58 (0.07)	1.65 (0.07)	1.66 (0.06)	1.70 (0.05)	1.75 (0.06)
$\text{P}_2\text{O}_5$	0.18 (0.05)	0.18 (0.05)	0.18 (0.05)	0.16 (0.05)	0.04 (0.03)
$\text{Fe}^{3+}/\text{Fe}_{\text{tot}}^b$	0.64 (0.03)	0.27 (0.03)	0.71 (0.03)	0.74 (0.03)	–
$\text{NBO}/T^c$	0.34	0.31	0.34	0.27	0.16
$K/G^d$	1.57 (0.02)	1.57 (0.02)	1.58 (0.02)	1.53 (0.02)	1.48 (0.02)
$T_g^e$ (°C)	654 (1)	645 (1)	662 (1)	696 (1)	737 (1)
$m^f$	30.5 (1)	30.5 (1)	30.5 (1)	31 (0.6)	31.8 (0.2)

<sup>a</sup>Electron microprobe average chemical composition ( $n = 10$ ). Parentheses represent  $\pm 1\sigma$ .

<sup>b</sup>From Mössbauer spectroscopy. Ratios were derived using MossA software<sup>95</sup>. Numbers in parentheses represent  $\pm 1\sigma$ .

<sup>c</sup> $\text{NBO}/T$  calculated after Prata et al.<sup>107</sup>.

<sup>d</sup>From Brillouin spectroscopy. Numbers in parentheses represent  $\pm 1\sigma$ .

<sup>e</sup>From C-DSC. Numbers in parentheses represent the experimental error.

<sup>f</sup>Fitted fragility using the Mauro–Yue–Ellison–Gupta–Allan (MYEGA) parametrization. Numbers in parentheses represent  $\pm 1\sigma$ .

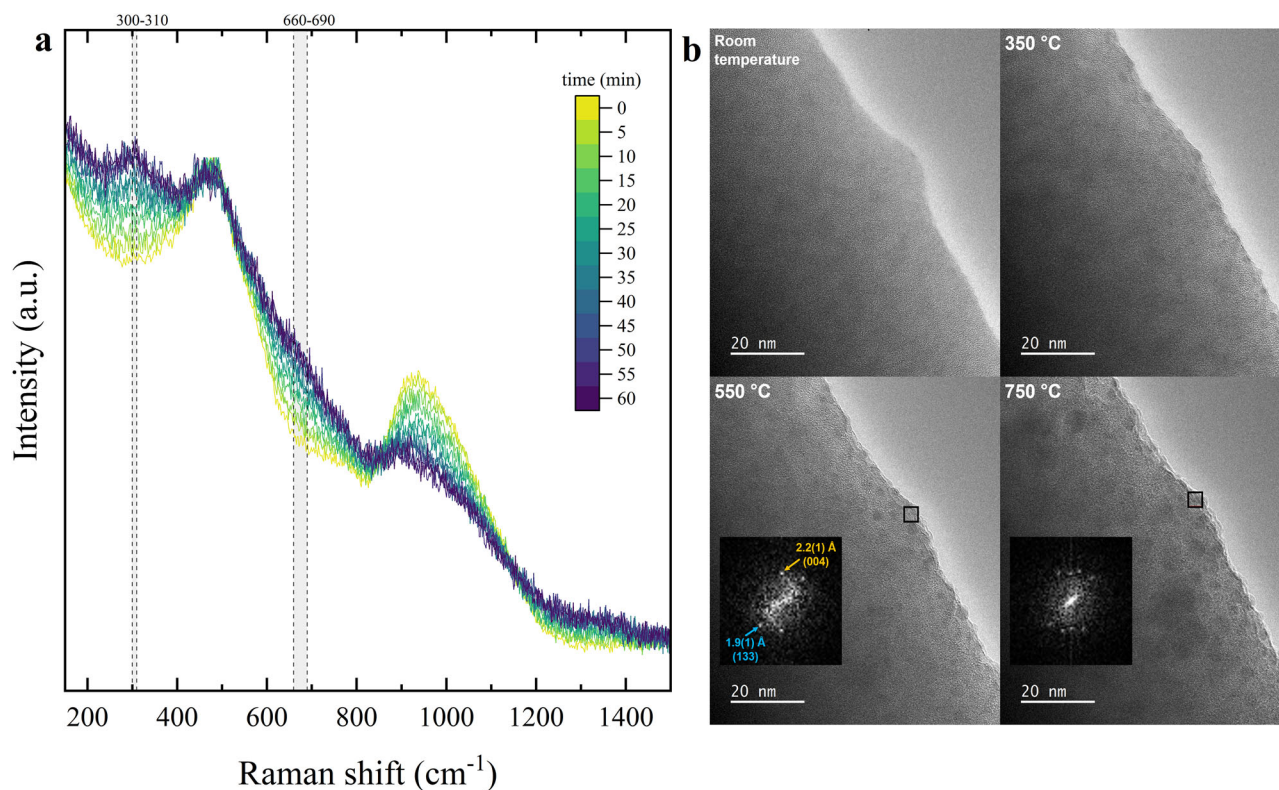


**Fig. 1 | In situ high-temperature results.** **a** Raman spectra evolution of sample AND100 at 723 °C revealing the formation of titanomagnetite crystals during an isothermal hold above  $T_g$  (654 °C; Table 1). Each colored curve represents 5 minutes. Shaded areas highlight the position of the most intense Raman features of titanomagnetite<sup>40,42–44</sup>. **b** Images acquired during in situ heating TEM experiment (Supplementary Movie), detailing the nanoscale evolution of AND100 from a

homogeneous amorphous glass to a heterogeneous amorphous material (350 °C), and then a nano-crystallized glass (550 °C and 750 °C). FFTs (insets) and post-experiment STEM-EDS (Supplementary Fig. 5) confirm the formed crystals to be magnetite-like. Temperatures (Supplementary Fig. 6) are affected by electron irradiation and should be therefore considered only in qualitative terms.

### The viscosity of homogeneous and crystal-free andesitic melts

High-temperature in situ measurements reveal the elevated reactivity of AND100 above its  $T_g$  (Fig. 1), highlighting the need for a meticulous experimental methodology to determine the melt viscosity<sup>20,21,52</sup>. To this end, we employed direct viscometry techniques, including micropenetration and concentric cylinder viscometry (Supplementary Micropenetration; Supplementary Concentric Cylinder). We further expanded our dataset by incorporating indirect viscosity estimates obtained from conventional and flash differential scanning calorimetry (C-DSC and F-DSC, respectively; Supplementary C-DSC; Supplementary F-DSC). To monitor potential sample alteration during measurements, such as crystallization and/or iron oxidation, we conducted Raman and Mössbauer spectroscopy before and after each experiment (Supplementary Preliminary Characterization; Supplementary C-DSC; Supplementary F-DSC; Supplementary Micropenetration; Supplementary Concentric Cylinder).

The accurate fitting of melt viscosity requires data from samples that preserved a homogeneous amorphous structure throughout all measurement stages. However, post-experiment Mössbauer and Raman results (Supplementary Preliminary Characterization; Supplementary C-DSC; Supplementary F-DSC; Supplementary Micropenetration; Supplementary Concentric Cylinder), as well as micropenetration (Fig. 2b) and post-micropenetration TEM results (Figs. 3, 4; Supplementary Figs. 11, 12 and 13), show that some viscosity measurements were affected by iron oxidation and titanomagnetite nanocrystallization during the experiments. Based on these observations, we exclusively used data from samples that remained nanolite-free after experiments to establish crystal-free viscosity parametrizations for our andesitic compositions (Supplementary Viscosity Parametrization). We accounted for iron oxidation by categorizing datasets according to the iron valence determined post-measurements. Combined with  $T_g$  values derived from C-DSC (Table 1; Supplementary C-DSC), we

applied the MYEGA parametrization (Eq. 5) using  $\log_{10}\eta_{\infty} = -2.93$ <sup>53,54</sup>, to fit the melt fragility index ( $m$ ). This allows us to characterize melt viscosity across a wide temperature range. Viscosity data from nanolite-free samples are shown as colored symbols in Fig. 2a, and the corresponding MYEGA fitting parameters are summarized in Table 1. To model andesite viscosity, we developed a calculator (provided as a Supplementary Data) applicable to compositions ranging from AND0 to AND100. This tool is based on the relationship between the transition metal content, glass transition temperature ( $T_g$ ), and fragility index ( $m$ ) (Supplementary Viscosity Parametrization).

Our results (Fig. 2a) show that the viscosity of homogeneous andesitic melts increases with decreasing transition metal oxide content progressing from AND100 to AND65, and then AND0. A 35% reduction in transition metal oxides ( $\text{FeO}_{\text{tot}}$ ,  $\text{TiO}_2$  and  $\text{MnO}$ ) from AND100 leads to an average viscosity increase of  $0.7 \pm 0.05 \log_{10}$  (approximately 5 times) at eruptive temperatures (900–1050 °C) relevant for Sakurajima volcano<sup>55</sup>. Complete removal of transition metal oxides (i.e., AND0) increases viscosity by  $\sim 1.5 \pm 0.1 \log_{10}$  ( $\sim 30$  times) at 900 °C and by  $\sim 1.1 \pm 0.1 \log_{10}$  ( $\sim 12$  times) at 1050 °C. Moreover, within the same temperature range, increasing the iron oxidation in AND100 (from  $\text{Fe}^{3+}/\text{Fe}_{\text{tot}} = 0.27$  to 0.71) results in a viscosity increase of  $\sim 2$  times (Supplementary Fig. 9), consistent with previous findings<sup>22,56,57</sup>.

It is important to note that these parametrizations apply specifically to homogeneous melts, free of nanolites or detectable nanoscale compositional heterogeneity in the amorphous state, as discussed further below. Our results indicate that the Giordano et al.<sup>39</sup> model overestimates the viscosity of AND100 ( $\text{GRD08}_{\text{AND100}}$ , Fig. 2b) by up to a factor of 25 at 700 °C and a factor of 3 at 900 °C. This discrepancy is not observed for the AND0 composition (Supplementary Fig. 9). These findings are consistent with Valdivia et al.<sup>20</sup>, who reported similar behavior for basaltic melts, suggesting

**Fig. 2 | Summary of viscosity results.** **a** Colored symbols represent nanolite-free viscosity data for a homogeneous melt (HOM). Solid lines illustrate MYEGA parametrizations for AND100, AND65 and AND0 (Table 1). **b** Impact of heterogeneities and iron oxidation state on the viscosity of AND100 compositions. White symbols represent nanolite-bearing viscosity data. The shaded grey region (heterogeneous melt, HET) represents the expected viscosity increase due to nanolite formation. Red arrows depict the isothermal rise in viscosity measured during micropenetration experiments at 660, 723 and 808 °C. The red dashed line shows the viscosity prediction for AND100 using the Giordano et al.<sup>39</sup> model. Experimental errors are smaller than symbol sizes.

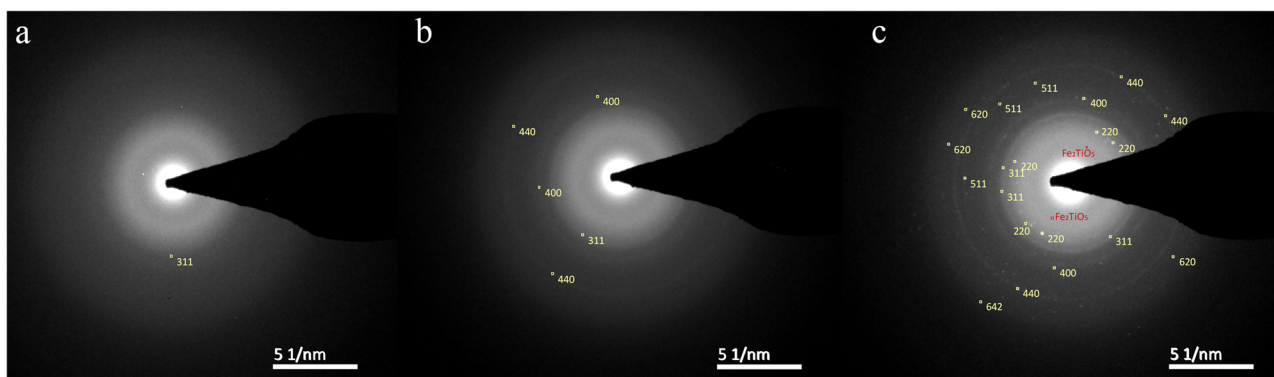
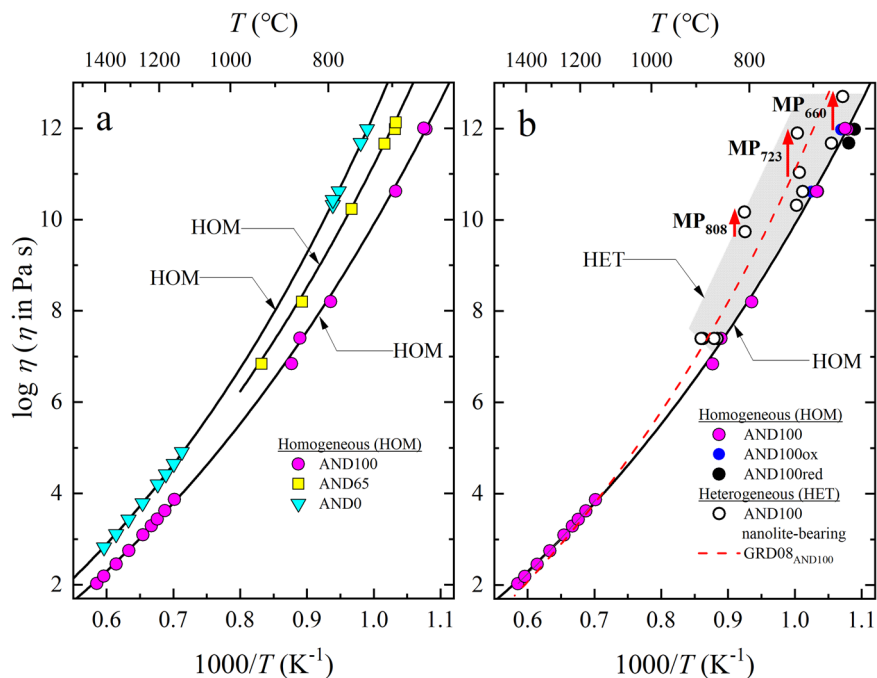


**Fig. 3 | Post-micropenetration (TEM) diffraction patterns of AND100 samples.** **a** MP<sub>660</sub>. **b** MP<sub>723</sub>. **c** MP<sub>808</sub>. Yellow indices correspond to the assignment of electron diffraction rings to specific lattice planes in the structure of titanomagnetite based on the respective *d*-spacings. The red points are the identification of a single spot associated with pseudobrookite (Fe<sub>2</sub>TiO<sub>5</sub>).

that the Giordano et al.<sup>39</sup> model may, for certain chemical domains, rely on viscosity data from melts containing nanoscale heterogeneities. Similarly, we observe deviations between our AND100 crystal-free parametrization and the nanolite-free viscosity data reported by Okumura et al.<sup>58</sup> (Supplementary Fig. 9), which also referenced the Giordano et al.<sup>39</sup> model.

### Nanoscale characterization of nanolite-bearing andesitic melts

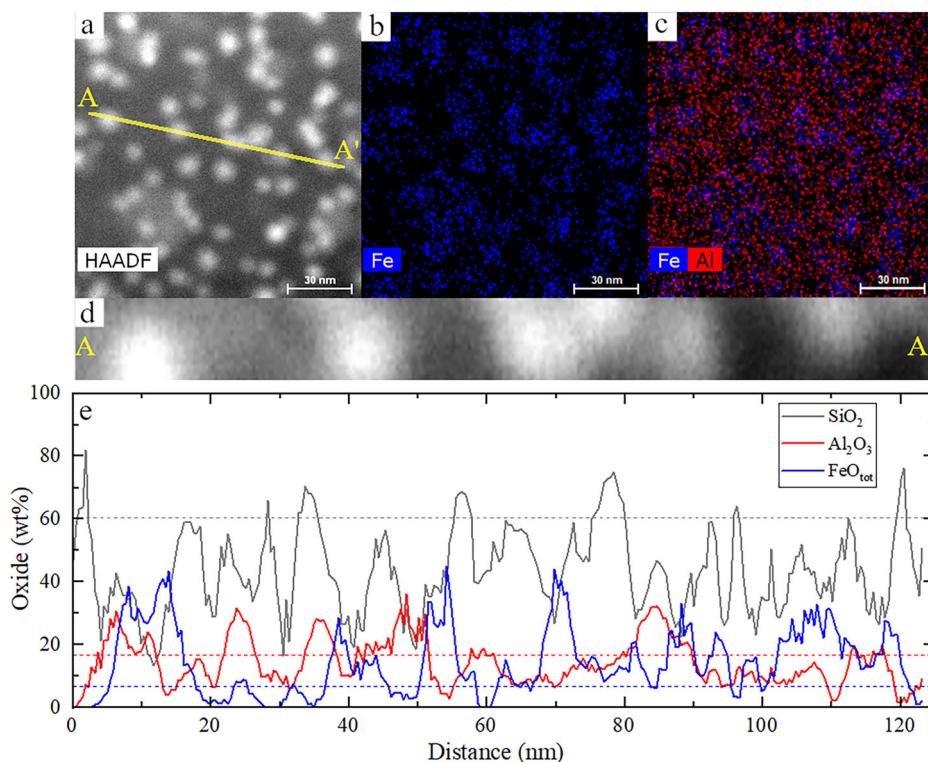
During micropenetration measurements on AND100 samples, we observed a time-dependent increase in viscosity at constant temperatures (Fig. 2b; Supplementary Micropenetration). Post-experiment analyses revealed that these changes were accompanied by nanocrystallization of titanomagnetite and iron oxidation. To investigate the mechanisms behind the viscosity increase, we conducted nanoscale characterization of the samples. We used room-temperature (S)TEM on FIB-prepared lamellas of known thickness (Table 2) to image the nanocrystals and obtain EDS chemical maps. To further assess nanoparticle size distribution and phase composition, we performed Small-Angle X-ray Scattering (SAXS) and Wide-Angle X-ray Scattering (WAXS) on 50 μm thick samples (see below).

Electron diffraction patterns (Fig. 3) and high-angle annular dark-field (HAADF) imaging (Fig. 4a), both acquired in TEM mode and STEM mode, respectively, confirmed the presence of nanocrystals. Selected area electron diffraction (SAED) patterns from post-micropenetration AND100 samples

are shown in Fig. 3. Most of the recorded *d*-spacings corresponds to the structure of titanomagnetite<sup>48,49,59</sup>. The diffraction patterns evolved from diffuse circular halos in sample AND100\_MP<sub>660</sub> to well-defined diffraction rings in AND100\_MP<sub>723</sub>, and especially in AND100\_MP<sub>808</sub> (Fig. 3). Notably, AND100\_MP<sub>808</sub> shows more pronounced diffraction features along the rings, indicating the presence of larger and more ordered nanocrystals. In particular, AND100\_MP<sub>660</sub> displays one diffraction ring (*d* = 2.53(1) Å) which matches the most intense reflection of titanomagnetite<sup>48,59</sup>, corresponding to the (311) plane (Fig. 3a). In AND100\_MP<sub>723</sub>, two additional low-intensity rings appear, with *d*-spacings of 1.48(5) and 2.09(9) Å, assignable to the (440) and (400) planes, respectively<sup>48,49,59</sup> (Fig. 3b). These three diffraction rings become more pronounced in AND100\_MP<sub>808</sub> and are accompanied by weaker ones assignable to the (220), (511), (620), and (642) planes<sup>48</sup> (Fig. 3c). Additionally, a single diffraction spot consistent with the (021) plane of pseudobrookite (Fe<sub>2</sub>TiO<sub>5</sub>, *d*-spacing = 4.3(1) Å) is uniquely observed in sample AND100\_MP<sub>808</sub> (Fig. 3c)<sup>60,61</sup>.

Nanolites are recognizable in STEM-HAADF images (Fig. 4a) by their bright contrast, consistent with their higher density relative to the surrounding matrix. Elemental maps (Fig. 4b) show that these particles are Fe-rich, in agreement with previous analyses (Supplementary Fig. 5). Conversely, aluminum (Al) is preferentially concentrated around these

**Fig. 4 | Nanoscale local variations in chemistry for AND100\_MP<sub>808</sub>.** **a** STEM-HAADF image of the sample. The bright pixels represent the crystalline phase. **b** EDS elemental distribution map of Fe. **c** EDS elemental distribution map of Fe+Al showing a preferential distribution of Al around Fe-rich nanolites. **d** Magnification of A-A' EDS-line-scan. **e** EDS line profile (A-A') results, with SiO<sub>2</sub>, Al<sub>2</sub>O<sub>3</sub> and FeO<sub>tot</sub> concentrations in wt%. Values on the x-axis represent the distance along the line profile (A-A'). Values on the y-axis represent the average composition of 7 neighboring pixels along the y-axis in **d**.



nanolites, creating Al-depleted zones between them. This distribution becomes especially evident when Fe and Al elemental maps are overlapped (Fig. 4c). To quantify local chemical variations, we extracted a representative STEM-EDS linescan across the sample (Fig. 4d). The resulting profile (Fig. 4e) confirmed the presence of Al-enriched halos surrounding Fe-rich nanolites. We also observed localized SiO<sub>2</sub> enrichment in the residual melt, corresponding to the darker region in the STEM-HAADF images (Fig. 4a).

From STEM-HAADF images (Supplementary STEM-HAADF) obtained from lamellas of known thickness, we determined the minimum nanolite radius, volume fraction, and nanolite number density (NND), accounting for possible nanolite overlap in the axis perpendicular to the plane of view. The average minimum nanolite radius increases from  $1.4 \pm 0.5$  to  $2.6 \pm 0.8$  nm as the temperature during viscosity measurements increases from 660 to 808 °C, with a progressive increase in nanolite content from  $0.51 \pm 0.1$  to  $2.45 \pm 0.1$  vol% (Table 2). This trend is consistent with Raman spectroscopy and electron diffraction results (Fig. 3; Supplementary Fig. 4) as well as high-temperature in situ experiments (Fig. 1; Supplementary Fig. 4), indicating that nanolite nucleation and growth become more pronounced as temperature increases above the glass transition.

To explore the temperature dependence of compositional heterogeneity, we quantified the average composition of four sub-regions: (1) the bulk image, (2) the nanolites, (3) the nanolites plus surrounding halos, and (4) the residual amorphous matrix (Fig. 5). Due to sample thickness (Table 2), compositions for nanolites and halos include a contribution from the surrounding amorphous matrix. The bulk STEM-EDS composition agrees well with the electron microprobe data for the AND100 starting material (Tables 1, 2), indicating minimal alkali migration during EDS analysis. Figure 5 illustrates the relative compositional differences of each sub-region normalized to the bulk composition (Table 2).

All three samples exhibit SiO<sub>2</sub> enrichment in the residual matrix, with average values near 70 wt% (Table 2), which is ca. 10 wt% higher than in the original AND100 composition and ca. 4 wt% higher than in the iron-free AND0 (Table 1). Conversely, Al<sub>2</sub>O<sub>3</sub> and FeO<sub>tot</sub> concentrations in the matrix decrease progressively as temperature increases from 660 to 808 °C. In parallel, FeO<sub>tot</sub> concentrations increase within the nanolites, consistent with titanomagnetite growth observed in our in situ experiments (Fig. 1).

Notably, during the early stages of nanolite formation (660 °C), we observed that they coexist with a diffuse, high-contrast phase (Supplementary Post-micropenetration STEM-EDS) and show an initial Al<sub>2</sub>O<sub>3</sub> enrichment (Fig. 5c), potentially reflecting a transient immiscibility between two aluminosilicate melts. At higher temperatures (808 °C), Al is expelled from the developing nanolites as more ordered titanomagnetite nanolites form (Fig. 5c). We infer that this process explains the observed Al accumulation around nanocrystals (Fig. 4; Supplementary Fig. 5) which is consistent with low mobility of Al in SiO<sub>2</sub>-rich liquids<sup>62</sup>.

This mechanism aligns with the titanomagnetite nanocrystallization pathway proposed for the 2018–2021 Fani Maoré lavas<sup>51</sup>, where nanolites formed from an Fe-rich immiscible melt<sup>63</sup>. It is also consistent with well-established observations in glass-ceramic materials, where Al-enriched shells are observed to surround the TiO<sub>2</sub>- and/or ZrO<sub>2</sub>- bearing nanocrystals that serve as crystallization seeds during subsequent heating<sup>64,65</sup>. Additionally, recent tracer diffusion experiments in TiO<sub>2</sub>-containing albitic glass demonstrate that Al mobility in supercooled aluminosilicate melts is enhanced by the presence of transition metals<sup>66</sup>, supporting a crystal nucleation mechanism involving the coupled diffusion of Al, Fe, and Ti.

To investigate nanoparticle distribution and crystallinity, we conducted SAXS and WAXS analyses. SAXS is sensitive to nanoscale electron density variations and provides information on particle size distributions, while WAXS captures scattering at larger angles, offering insights into long-range structural order and crystalline phases<sup>67</sup>. SAXS results (Fig. 6a) indicate the presence of a spherical phase with different density with respect to the matrix, and changes in the spherical particle size and distribution with temperature (SAXS parameters in Supplementary Table 4). The SAXS signal shifts from a peak at  $\sim 0.9$  nm<sup>-1</sup> for the 660 °C sample to  $\sim 0.5$  nm<sup>-1</sup> for the 723 °C sample. In the 808 °C sample, the scattering pattern changes markedly, showing at least two distinct contributions: one centered at  $\sim 0.5$  nm<sup>-1</sup>, as observed at 723 °C, and a second, broader feature emerging at lower  $q$  ( $\sim 0.1$  nm<sup>-1</sup>), indicating the presence of two separate phases.

SAXS fitting results show a decrease in the Porod parameter from  $0.14 \times 10^{-4}$  for the 660 °C sample to  $0.24 \times 10^{-6}$  for the 723 °C sample, indicating that the particles are relatively isolated, with limited aggregation and simple surface morphology. Due to the restricted  $q$ -range at low  $q$

**Table 2 | Post-micropenetration STEM-EDS<sup>a</sup> (wt%), HAADF image analysis<sup>b</sup> and SAXS/WAXS results for AND100 samples**

	AND100_MP <sub>660</sub>				AND100_MP <sub>723</sub>				AND100_MP <sub>808</sub>							
	Bulk <sub>TEM</sub>	Matrix <sub>TEM</sub>	Nanolite <sub>TEM</sub>	Nanolite + Halo <sub>TEM</sub>	Bulk <sub>TEM</sub>	Matrix <sub>TEM</sub>	Nanolite <sub>TEM</sub>	Nanolite + Halo <sub>TEM</sub>	Bulk <sub>TEM</sub>	Matrix <sub>TEM</sub>	Nanolite <sub>TEM</sub>	Nanolite + Halo <sub>TEM</sub>	Bulk <sub>TEM</sub>	Matrix <sub>TEM</sub>	Nanolite <sub>TEM</sub>	Nanolite + Halo <sub>TEM</sub>
SiO <sub>2</sub>	61.8	70 (9)	55 (9)	60 (3)	62.7	71 (5)	53 (9)	60 (3)	60.4	70 (3)	44 (10)	58 (4)				
TiO <sub>2</sub>	0.7	0.5 (1)	0.8 (1)	1 (1)	0.8	0.8 (0.9)	2.5 (6)	1.1 (0.5)	1.1	0.6 (0.9)	2.9 (2)	1.4 (0.5)				
Al <sub>2</sub> O <sub>3</sub>	17.5	16 (7)	21 (7)	20 (4)	17.4	16 (4.8)	18 (7)	18 (1.4)	16.7	14 (3.4)	16.1 (7)	18.5 (1.4)				
FeO <sub>tot</sub>	7.1	6.9 (6)	10.6 (6)	8 (2)	7.1	2.8 (1.6)	13 (6)	8.4 (2)	7.2	1.7 (1.7)	22 (5)	11 (2)				
MgO	3.0	3.1 (5)	4.3 (6)	2.8 (1.5)	2.8	2 (1.4)	2.4 (2.7)	3.1 (0.9)	2.8	2.2 (1.9)	4 (3)	3.4 (1)				
CaO	5.7	3.6 (2.7)	6.1 (3.5)	6.3 (2.3)	6.1	4.7 (1.9)	7.2 (4)	6.8 (4)	7.0	6.3 (2.1)	8 (4)	7.8 (1)				
Na <sub>2</sub> O	1.3	0.5 (1)	0.7 (1)	0.5 (0.5)	0.8	0.4 (0.6)	1.4 (3)	0.5 (0.4)	2.5	2 (1.6)	1 (1)	0.9 (0.8)				
K <sub>2</sub> O	2.3	0.9 (1)	0.8 (1)	0.6 (0.6)	2.0	0.8 (0.9)	1.3 (2)	0.9 (0.6)	2.3	1.7 (1.1)	0.8 (1)	1 (1)				
P <sub>2</sub> O <sub>5</sub>	0.60	1.2 (2)	1.3 (2)	0.8 (1)	0.20	1 (0.6)	0.7 (2)	0.4 (0.6)	2.29	0.9 (1)	1 (0.9)	1 (1)				
n =	1	40	23	20	1	22	40	6	1	13	37	8				
radius <sub>TEM</sub> <sup>b</sup> (nm)	1.39 (0.55) ROIs = 4002															
lamella thickness (nm)	50 (2)															
nanolite content (vol%)	0.51 (0.1)															
NND <sup>c</sup> (nm <sup>-3</sup> ) × 10 <sup>4</sup>	2.93															
radius <sub>SAXS</sub> <sup>d</sup> (nm)	1.7 (0.02)															
size <sub>WAXS</sub> <sup>d</sup> (nm)	-															
<sup>a</sup> Parenttheses in STEM-EDS results represent 1±σ. Bulk <sub>TEM</sub> measurements have an error margin of 2% of the measured value. <sup>b</sup> More details in Supplementary STEM-HAADF. <sup>c</sup> NND: nanolite number density. The amount of nanolites per volume. <sup>d</sup> More details in Supplementary SAXS-WAXS. Parenthesis represents the fit error. <sup>e</sup> More details in Supplementary Fig. 14. Parenthesis represents the fit error.																
$R_1 = 14 (1)$ $R_2 = 3.8 (0.5)$ $D_{\text{pyroxene}} = 19.2 (0.5)$ $D_{\text{titanomaghemite}} = 6.7 (0.5)$																

**Fig. 5 | STEM-EDS local chemistry for each sub-region.** **a** Residual amorphous matrix. **b** Nanolites and the compositionally differentiated halo surrounding them. **c** Nanolite cores. Average values were normalized to the bulk composition of the sample ( $Bulk_{TEM}$  in Table 2). The data was obtained from the analysis of STEM-EDS maps (Supplementary Figs. 11, 12 and 13) performed on samples treated at 660 °C, 723 °C and 808 °C during viscosity measurements. Error bars correspond to  $\pm 1\sigma$  (Table 2).

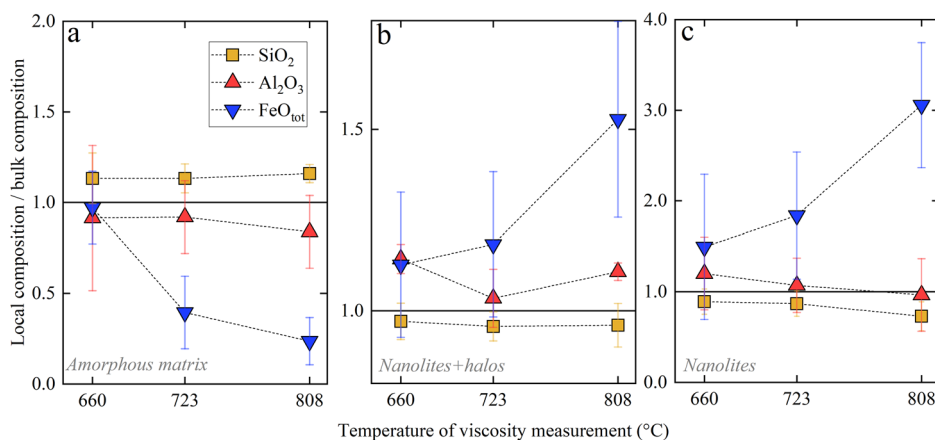
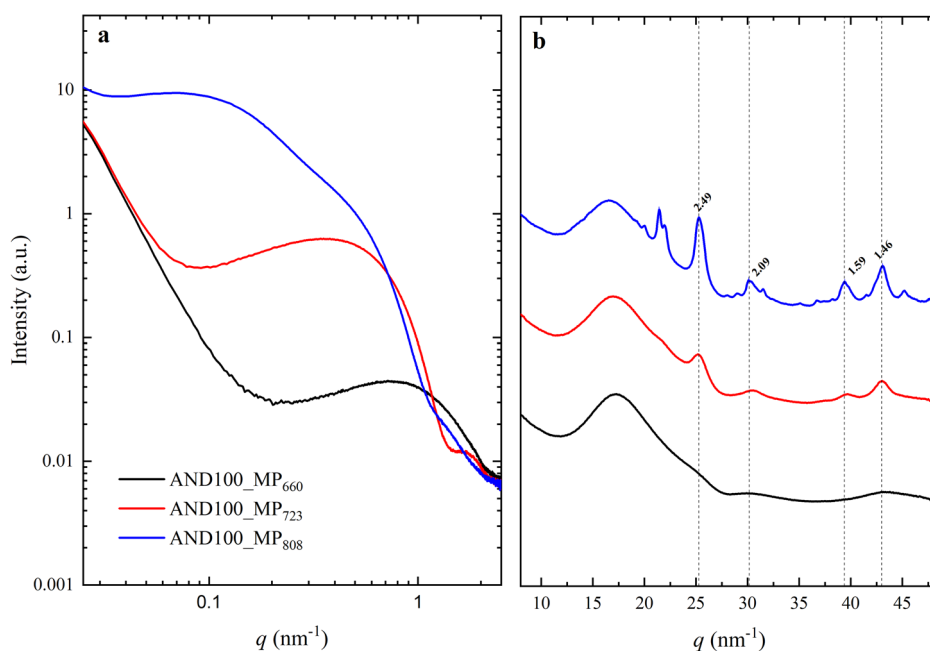


**Fig. 6 | SAXS-WAXS analyses of post-micropenetration AND100 samples.** **a** SAXS results. The fit SAXS parameters used for the modelling of particle size are reported in Supplementary Table 4. **b** WAXS results. The numbers above the peaks correspond to the calculated  $d$ -spacing (Å) using Eq. 18, where dashed lines correspond to peaks assignable to titanomagnetite<sup>40,42–44</sup>. MP<sub>660</sub> was X-ray amorphous, while AND100\_MP<sub>723</sub> exhibited diffraction peaks assignable to titanomagnetite and AND100\_MP<sub>808</sub> contained titanomagnetite + pyroxene.



values, the Porod parameter estimated for the 808 °C sample (0.12) is not considered reliable. The extracted fractal dimension ( $fract = 3.75 \pm 0.25$ ; Supplementary Table 4) is consistent with spherical particle geometry. The structure factor ( $\eta_{HS}$ , Supplementary Table 4) is approximately 0.1 for the AND100\_MP<sub>660</sub> and AND100\_MP<sub>723</sub> samples, but decreases to  $\sim 0$  for AND100\_MP<sub>808</sub>, indicating increased particle interaction and aggregation at higher temperature. Overall, the temperature-dependent shift of the SAXS signal toward lower  $q$  values suggests an increase in particle size, accompanied by more complex surface features and a higher degree of aggregation at elevated temperature.

SAXS modelling for AND100\_MP<sub>660</sub> yields an average radius of amorphous nanoheterogeneities (see WAXS description below) of  $1.7 \pm 0.02$  nm (Table 2). For AND100\_MP<sub>723</sub>, the average radius increases to  $3.1 \pm 0.1$  nm, corresponding to nanocrystals as identified in WAXS. SAXS analysis of AND100\_MP<sub>808</sub> reveals a dominant population with average radii of  $3.8 \pm 0.5$  nm. These values are consistent with STEM-HAADF image analysis, which shows an increase in the average nanoheterogeneity radius from  $1.4 \pm 0.5$  nm to  $2.6 \pm 0.8$  nm (Table 2).

WAXS analysis provides complementary information on crystallinity and phase composition over larger volumes than those probed by TEM. The WAXS pattern of AND100\_MP<sub>660</sub> (Fig. 6b) lacks sharp diffraction features,

indicating the absence of long-range order and the presence of nanoscale amorphous phase separation. This is consistent with SAXS data showing isolated particles with minimal aggregation and with the diffuse TEM diffraction patterns observed in Fig. 3a. For AND100\_MP<sub>723</sub>, WAXS patterns display distinct diffraction peaks corresponding to titanomagnetite<sup>48,49,59</sup>, with  $d$ -spacings assignable to the (311), (400), (511), and (440) crystallographic planes. These observations match the TEM diffraction results for this sample, indicating the onset of crystalline phase formation.

The WAXS pattern for AND100\_MP<sub>808</sub> reveals a more complex phase assemblage, including both titanomagnetite<sup>48,49,59</sup> and pyroxene<sup>68</sup>. Rietveld refinement shows that titanomagnetite crystals have an average crystal size of  $6.7 \pm 0.5$  nm, while pyroxene crystals measure approximately  $19.2 \pm 0.5$  nm (Table 2). These results are consistent with those reported by Mujin et al.<sup>37</sup>, who identified ferroaugite crystals measuring 20–30 nm and titanomagnetite particles ranging from 1 to 20 nm in pyroclasts from the 2011 Shinmoedake eruption.

Overall, the combined SAXS, WAXS, and TEM analyses provide a consistent and detailed picture of particle size evolution, phase composition, and crystallinity as a function of temperature at the nanoscale, demonstrating that our experimental results closely reflect natural magmatic processes.

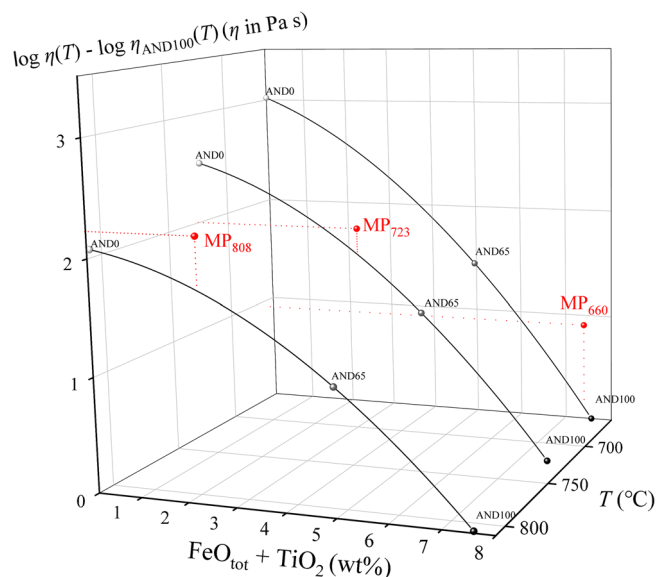


**Fig. 7 | Nanolite-bearing viscosity of AND100 samples.** Normalized viscosity as a function of temperature and  $\text{FeO}_{\text{tot}} + \text{TiO}_2$  content (wt%) of their STEM-EDS-derived residual matrix composition (Fig. 5; Table 2). Viscosity is normalized to the AND100 melt (Table 1; Fig. 2). The MP sub-index represents the temperature ( $^{\circ}\text{C}$ ) of micropenetration measurement. The black curves correspond to the viscosity as a function of  $\text{FeO}_{\text{tot}} + \text{TiO}_2$  content (wt%) at 660, 723 and 808  $^{\circ}\text{C}$  respectively. A viscosity calculator is provided as Supplementary Data.

### The viscosity of nanolite-bearing andesitic melts

To elucidate the impact of nanocrystallization and iron oxidation on the viscosity of andesitic melts, we compare our viscosity micropenetration results for AND100 samples with the corresponding melt viscosity parametrizations (Fig. 2b). For AND100\_MP<sub>660</sub>, the initial viscosity measurement ( $\eta = 10^{12}$  Pa s; Supplementary Table 2) closely matches the predicted melt viscosity of AND100 at 660  $^{\circ}\text{C}$ . However, a progressive increase in viscosity was observed under isothermal conditions, reaching a final value of  $\eta = 10^{12.7}$  Pa s, accompanied by a slight increase in the iron oxidation state to  $\text{Fe}^{3+}/\text{Fe}_{\text{tot}} = 0.7$ . This final viscosity is approximately 8 times higher than the predicted value for AND100 ( $\text{Fe}^{3+}/\text{Fe}_{\text{tot}} = 0.64$ ) at the same temperature. STEM-EDS data (Figs. 3 and 4; Table 2) show that less than 3 wt% of the total iron precipitated as nanocrystals in this sample. Thus, the presence of solid particles (<1 vol%; Table 2), as considered in classical particle suspension models<sup>69</sup>, and the overall compositional variations<sup>34,58</sup> (e.g., Fe-Ti removal in Fig. 7) of the surrounding amorphous phase are insufficient to account for the observed viscosity increase.

We propose that the rapid formation of a  $\text{SiO}_2$ -enriched matrix, the segregation of Fe-rich immiscible domains, and subsequent crystallization of titanomagnetite, leads to the development of a complex and heterogeneous nanostructure (Fig. 4). This structural evolution likely explains the excess measured viscosity, as illustrated in Fig. 7.

Similar trends are observed at higher temperatures. For AND100\_MP<sub>723</sub>, the final viscosity ( $\eta = 10^{11.9}$  Pa s;  $\text{Fe}^{3+}/\text{Fe}_{\text{tot}} = 0.79$ ) is nearly 5 times greater than the predicted viscosity of AND65 ( $\eta = 10^{11.18}$  Pa s) at 723  $^{\circ}\text{C}$ , even though the residual matrix retains approximately 40% of the initial  $\text{FeO}_{\text{tot}}$  content (Table 2). For AND100\_MP<sub>808</sub>, the final viscosity ( $\eta = 10^{10.17}$  Pa s;  $\text{Fe}^{3+}/\text{Fe}_{\text{tot}} = 0.83$ ) slightly exceeds the predicted viscosity of AND0 at 808  $^{\circ}\text{C}$  ( $\eta = 10^{10}$ ; Fig. 2), despite the residual matrix still containing ~25% of the original  $\text{FeO}_{\text{tot}}$  (Fig. 5; Table 2).

It should be noted that complete precipitation of  $\text{FeO}_{\text{tot}}$  as crystalline phases is unlikely during the experiment, as the temperature-dependent solubility of  $\text{FeO}_{\text{tot}}$  in the metastable melt is not expected to approach zero, even under deep supercooling<sup>70</sup>. Even in the comparatively evolved AND100\_MP<sub>808</sub>, the crystalline phase content (~2.45 vol%) is too low

to significantly affect melt viscosity through conventional suspension mechanisms<sup>69</sup>.

Overall, our findings highlight the complex interplay of nanocrystallization, iron oxidation, and nanoscale phase separation in controlling the rheology of andesitic melts. While previous studies<sup>19,33</sup> attributed the viscosity increase solely to iron depletion in the residual aluminosilicate matrix due to titanomagnetite nanocrystallization, our results suggest a more complex mechanism. We propose that the rapid segregation of nanoscale Fe-rich immiscible droplets initiates the formation of a relatively  $\text{SiO}_2$ -enriched matrix. Titanomagnetite nanocrystallization then occurs within these Fe-rich domains. As the nanocrystals grow and develop long-range order, aluminum is expelled from the crystal structure, forming Al-enriched shells around the nanolites.

Additionally, post-micropenetration Mössbauer spectroscopy (Supplementary Micropenetration; Supplementary Table 2) shows that the  $\text{Fe}^{3+}/\text{Fe}_{\text{tot}}$  ratios of the AND100 samples exceed the stoichiometric requirement for titanomagnetite to consume all the iron in the melt. This indicates that in samples such as AND100\_MP<sub>723</sub> and AND100\_MP<sub>808</sub>, which contain well-developed titanomagnetite nanolites, a significant portion of the remaining iron in the  $\text{SiO}_2$ -enriched matrix likely exists as  $\text{Fe}^{3+}$ . This oxidation state may enhance the polymerization of the residual melt structure by converting network-modifying cations into charge-compensating species and promoting  $\text{Fe}^{3+}$  as a network-forming component<sup>57,71–73</sup>.

Notably, nanolite formation was observed under various oxygen fugacity conditions during our high-temperature experiments. This observation aligns with previous work<sup>40,74</sup>, which shows that nanolites can form across a broad range of redox conditions relevant to both natural magmatic environments and experimental settings.

As discussed above, and accounting for Fe-Ti extraction due to nanocrystallization, we observe a consistent surplus in viscosity across all our nanolite-bearing samples, ranging from 2 to 6 times higher than the expected values for homogeneous melts (Fig. 7). Notably, nanoscale chemical heterogeneity has the greatest impact at low crystal fractions, as seen in MP<sub>660</sub> (Fig. 7), where the pronounced viscosity increase cannot be explained solely by Fe-Ti depletion, crystal suspension, or aggregation. Bulk Fe-Ti extraction appears to play a more significant role at low to moderate crystal fractions, such as in MP<sub>723</sub>, where the initial melt viscosity is comparatively lower.

At higher nanolite contents, as in MP<sub>808</sub> (Fig. 7), SAXS data indicate the emergence of particle interaction, introducing an additional mechanism influencing viscosity during magmatic crystallization. This interaction likely arises from pervasive nanoscale heterogeneity driven by the concurrent diffusion and segregation of elements such as Al, Ti, and Fe (Figs. 4, 5; Table 2), in response to iron oxidation and titanomagnetite nanocrystallization<sup>75</sup>. These processes lead to the formation of chemically distinct nanodomains in the initially homogeneous melt, including nano-sized crystals, Al-enriched shells, and highly  $\text{SiO}_2$ -enriched regions (up to ~70 wt%; Fig. 5; Table 2), significantly increasing the effective bulk viscosity (Fig. 2b).

The nanolite-bearing viscosity of AND100\_MP<sub>808</sub> (Fig. 7) indicates that the viscosity of AND0, a homogeneous melt devoid of transition metals, only provides a lower bound for the viscosity of nanolite-bearing AND100 at temperatures above 808  $^{\circ}\text{C}$ . At these conditions, compositional fluctuations and particle interactions at the nanoscale become increasingly pronounced (Fig. 5).

These findings demonstrate that the physical properties of titanomagnetite-bearing silicate melts cannot be directly compared with those of homogeneous materials without a critical assessment of data reliability. We show that nanolite nucleation and growth result in chemically differentiated nanodomains that induce a complex and substantial increase in viscosity. For example, progressive titanomagnetite crystallization is accompanied by a systematic increase in DSC-derived characteristic temperatures (Supplementary C-DSC; Supplementary F-DSC). Despite the relatively low titanomagnetite content typically observed in natural melts, its effect on viscosity should not be underestimated.

Consistent with previous research<sup>28,35,36,76</sup>, our findings suggest that the viscosity increase induced by nanocrystallization, and modulated by the formation of chemical heterogeneities at the nanoscale, may influence eruption dynamics. These results have important implications for understanding the behavior of andesitic magmas, which are characterized by diverse eruptive styles<sup>77</sup>. Rapid magma ascent can generate high undercooling, promoting syn-eruptive crystallization within volcanic conduits<sup>10</sup>. This is known to enhance the coupling between gas and melt, potentially affecting the dynamics of magma ascent. Additionally, melt dehydration, oxidation, and thermal fluctuations during magma ascent may also lead to nanocrystallization in the shallow conduit<sup>29,30,32</sup>.

Importantly, nanocrystallization not only increases magma viscosity, but it can also facilitate the formation of nucleation sites for gas bubbles<sup>36,78</sup>, thereby hindering bubble connectivity and outgassing. We hypothesize that the formation of the documented heterogeneous texture composed of melt and (nano)crystalline phases may have a non-trivial impact on water exsolution. The development of nanoscale heterogeneities may locally elevate water concentration and induce supersaturation, as nanolites cannot accommodate volatiles, thereby “squeezing” water out of the surrounding melt. Additionally, this study also contributes to a better understanding of the evolving physical properties of andesitic domes and plugs, as they are known to be exposed to naturally occurring reheating processes<sup>79</sup>.

Together, these effects could potentially act as a gateway for magma fragmentation<sup>13</sup>, explaining the explosivity of andesitic magmas<sup>80</sup>. Supporting this, a recent study<sup>81</sup> identified nanoscale Al-rich heterogeneities on the surfaces of natural andesitic ash particles, indicating that ash-forming fractures preferentially propagate through regions surrounding Fe-rich nanolites. This mechanism for fracture propagation is consistent with the formation of chemically differentiated nanodomains, as magma failure should propagate through the most viscous zones (i.e., the SiO<sub>2</sub>-enriched matrix), resulting in Al-rich surfaces in the ash particles.

In summary, the formation of nanolites and associated chemical heterogeneity drives rheological changes in andesitic magma, influencing ascent dynamics and contributing to variations in eruptive style.

## Conclusions

We present, to the best of our knowledge, the first in situ observation of nanolite formation in a synthetic andesitic melt and introduce viscosity models tailored to various andesitic compositions. Our observations show that iron oxidation and nanocrystallization readily occur above the glass transition temperature. This challenges conventional interpretations, as the observed viscosity increase due to titanomagnetite nanocrystallization cannot be explained solely by iron depletion in the residual amorphous matrix or by the presence of solid particles. Instead, we propose a more complex mechanism: rapid amorphous phase separation leads to the formation of nanoscale Fe-rich domains, inducing relative SiO<sub>2</sub> enrichment in the surrounding matrix. Titanomagnetite nanocrystallization then proceeds within these Fe-rich domains. As these titanomagnetite nuclei grow, aluminum is expelled from the crystalline nuclei, forming Al-enriched shells surrounding the nanolites. This sequence of events results in a viscosity increase of up to 30 times at eruptive temperatures. This increased magma viscosity, coupled with an inherently non-uniform mechanical response due to its nanoscale chemical heterogeneity, may significantly influence the rheological properties of the melt and, consequently, the eruption dynamics of andesitic volcanoes.

## Materials and methods

### Synthesis of starting glasses

AND100, AND65 and AND0 were synthesized by mixing powder reagents (SiO<sub>2</sub>, TiO<sub>2</sub>, Al<sub>2</sub>O<sub>3</sub>, Fe<sub>2</sub>O<sub>3</sub>, MnO, MgO, CaCO<sub>3</sub>, Na<sub>2</sub>CO<sub>3</sub>, K<sub>2</sub>CO<sub>3</sub>, and P<sub>2</sub>O<sub>5</sub>) according to their target compositions. The mass of each oxide and carbonate component was determined through molar mass calculations. All reagents were mixed using an agate mortar and ethanol. The mixture underwent manual grinding for ~45 min before being dried using an infrared light. Subsequently, the dry mixture was placed in an alumina

crucible and subjected to an overnight heat treatment at 900 °C to eliminate CO<sub>2</sub> from the carbonate compounds. Following decarbonization, the material was transferred to a Pt crucible and melted for 24 h at 1400 °C. Afterwards, the melt was rapidly quenched in water to prevent crystallization. The resulting quenched glass was crushed to powder using a stainless-steel percussion mortar and then manually mixed before performing a second melting to achieve chemical homogenization. The second round of melting at 1400 °C lasted for 4 h, after which the crucible was swiftly immersed in water for rapid cooling. Subsequently, AND100red was produced by re-melting AND100 sample in a hanging Au<sub>80</sub>Pd<sub>20</sub> open capsule at 1275 °C and 1 atm for 24 h, using a gas mixing furnace with a gas mixture of 95% CO<sub>2</sub> and 5% CO. The resulting melt was rapidly quenched in water by melting the Pt wire.

### Electron microprobe analyses (EMPA)

The major elemental composition (Si, Ti, Al, Fe<sub>tot</sub>, Mn, Mg, Ca, Na, K, and P) of samples AND100, AND100ox, AND100red, AND65, and AND0 was determined using a JEOL JXA-8200 electron microprobe at the Bayerisches Geoinstitut (University of Bayreuth, Germany) (Table 1). Glasses were embedded in epoxy, polished, and carbon coated. Measurements were performed using 15 kV voltage, 5 nA current, and 20 s of counting time under a defocused 10 μm beam. We collected 10 points per sample to account for heterogeneities. Synthetic wollastonite (Ca, Si), periclase (Mg), hematite (Fe), spinel (Al), orthoclase (K), albite (Na), manganese titanate (Mn, Ti), and apatite (P) were used as calibration standards. Sodium and potassium were analyzed first to mitigate alkali migration effects<sup>82</sup>.

### Micropenetration viscometry

We conducted micropenetration (MP) viscometry measurements on plane-parallel and polished glass chips of 2–3 mm in thickness. These measurements were carried out utilizing a vertical dilatometer (Bähr VIS 404) at the Institute of Non-Metallic Materials, TU Clausthal (Germany). We measured the indentation rate of a sapphire sphere ( $r = 0.75$  mm) during isothermal dwells at temperatures controlled using an S-type thermocouple (Pt-PtRh) placed at ~1.5 mm from the sample surface. The temperature error is estimated to be ±2 °C considering the accuracy of the S-type thermocouple and its distance from the sample<sup>83</sup>. We followed standard procedures<sup>20,21,40,84</sup> to achieve thermal equilibration at the target temperature. The indentation depth was measured as a function of time and the viscosity curve was determined according to Eq. 1<sup>85</sup>:

$$\eta = \frac{3F}{16\sqrt{2rL} \frac{dl}{dt}} \quad (1)$$

where  $\eta$  is the Newtonian viscosity (Pa s),  $F$  is the applied force (N),  $t$  is the time (s),  $r$  is the radius of the sphere (m),  $L$  is the cumulative indentation depth (m), and  $\frac{dl}{dt}$  is the indentation within a measurement interval. The dilatometer was previously calibrated using a standard glass DGG-1, reproducing the certified viscosity data<sup>86</sup> with a deviation of ± 0.1 in log units. Data points are reported in the text according to the scheme *SampleName*\_MP<sub>Temperature</sub>, with temperature representing the final experimental temperature expressed in °C, and the duration in minutes.

### Concentric cylinder (CC) viscometry

High-temperature viscosity measurements were conducted using a Rheometric II Rotational Viscometer (Theta Instruments) at the Experimental Volcanology and Petrology Laboratory (EVPLab, Roma Tre University, Italy). The experimental apparatus featured an Anton Paar Rheolab Qc viscometer head with a maximum torque capacity of 75 mN m<sup>87</sup>. Temperature monitoring was carried out using a factory-calibrated S-type thermocouple, with a precision of ±2 °C. The concentric cylinder was previously calibrated using a standard glass NIST 717a, reproducing the certified viscosity data with a deviation of ± 0.03 in log units<sup>88</sup>. To ensure thorough thermo-chemical homogenization, the glass materials were loaded into a Pt<sub>80</sub>Rh<sub>20</sub> cylindrical crucible (62 mm in height, and 32 mm inner

diameter) and stirred at  $\dot{\gamma} = 10 \text{ s}^{-1}$  using a Pt<sub>80</sub>Rh<sub>20</sub> spindle (3.2 and 42 mm in diameter and length, respectively) at 1435 °C at air oxygen fugacity and ambient pressure for 5 hours. Subsequently, the temperature was lowered by steps of 25–50 °C down to 1150 and 1130 °C for the samples AND100ox and AND0, respectively. The viscosity was measured at every step, holding the conditions constant until steady viscosity and temperature values had been achieved (~45 min). At the end of the experiments, the temperature was quickly raised to 1430 °C where a portion of the melt was rapidly quenched in water to determine the iron oxidation state of the high-temperature viscosity measurements.

### Differential scanning calorimetry

Conventional differential scanning calorimetry (C-DSC) measurements were performed at the Institute of Non-Metallic Materials, TU Clausthal (Germany). Around 15 mg ( $\pm 5$ ) of glass was placed in a Pt<sub>80</sub>Rh<sub>20</sub> crucible under a constant N<sub>2</sub> (5.0) flow rate of 20 ml min<sup>-1</sup>. We used two conventional differential scanning calorimeters (C-DSC, 404 F3 Pegasus and 404 cell, Netzsch) to measure the heat flow at a heating rate ( $q_h$ ) of 10 and 20 °C min<sup>-1</sup>. Additionally, we used ~50 ng of glass to perform flash differential scanning calorimetry (F-DSC) analyses, using a Flash DSC 2+ (Mettler Toledo) equipped with UFH 1 sensors, under constant Ar 5.0 flow (40 ml min<sup>-1</sup>).

The C-DSC was calibrated using melting temperatures and enthalpy of fusion of reference materials (pure metals: In, Sn, Bi, Zn, Al, Ag, and Au), and the F-DSC was calibrated using the melting temperature of aluminum (660.3 °C) and indium (156.6 °C). In our C-DSC measurements, we employed the methodology outlined by Stabile et al.<sup>42</sup> Initially, we erased the thermal history of the glass by subjecting the sample to a two-step thermal treatment. This involved a first upscan at a rate of  $q_h = 20 \text{ °C min}^{-1}$  until it reached a temperature slightly above  $T_{peak}$ , namely  $T_{max}$ . Subsequently, we cooled the melt to 100 °C at rates of  $q_c = 10$  or  $20 \text{ °C min}^{-1}$ . The actual C-DSC measurements were then conducted using the rate-matching method, which entailed an additional upscan (matching heating segment) with a rate matching that of the preceding downscan (i.e.,  $q_h = q_c$ ). From the measured heat flow during the matching upscan, we extracted the characteristic temperatures  $T_{onset}$  and  $T_{peak}$ , both related to phase transitions or thermal events observed during the heating or cooling of a sample. For further details see the methodology presented in Valdivia et al.<sup>20</sup>

For F-DSC experiments, we followed the methodology described above employing a  $q_h = q_c = 1000 \text{ °C s}^{-1}$  (60000 °C min<sup>-1</sup>). Subsequently, we conducted a series of measurements on the same sample, using the same chip, at 10000 °C s<sup>-1</sup> (600000 °C min<sup>-1</sup>) to investigate the impact of nanocrystallization on the characteristic temperatures  $T_{onset}$  and  $T_{peak}$  due to consecutive thermal treatments.

Following the theoretical background discussed elsewhere<sup>40,89–91</sup>, viscosity values were derived from C- and F-DSC data using the relationship between the matching heating rate ( $q_h$ ) of the measurement and the shift factors  $K_{onset}$  and  $K_{peak}$ <sup>40,42</sup> expressed in Eq. 2:

$$\log_{10} \eta(T_{onset,peak}) = K_{onset,peak} - \log_{10}(q_h) \quad (2)$$

where  $K_{onset} = 11.20 \pm 0.15$  and  $K_{peak} = 9.84 \pm 0.20$ <sup>40,42</sup>. It is important to mention that when  $q_h$  is 10 °C min<sup>-1</sup>,  $\eta(T_{onset}) \approx 10^{12}$  Pa s, and therefore,  $T_{onset} \approx T_g$ . The validation of the shift factor method (Eq. 2) for our compositions is discussed in the Supplementary Viscosity Parametrization.

### Brillouin Spectroscopy

Brillouin spectroscopy (BLS) measurements were performed at the Bayerisches Geoinstitut (University of Bayreuth, Germany). Plane-parallel glass plates with a thickness of ~50 μm were analysed using a solid-state Nd:YVO<sub>4</sub> laser source operating at a wavelength of 532 nm and 50 mW power. The Brillouin frequency shift was quantified utilizing a six-pass Fabry–Perot interferometer<sup>92</sup> coupled with a single-pixel photon counter detector. Measurements were conducted using a symmetric forward scattering configuration<sup>92</sup> with a scattering angle of  $\theta = 79.8^\circ$ . The accuracy of

the scattering angle was established through calibration with a reference silica glass. Conversion of frequency shifts ( $\Delta\omega$ ) to longitudinal ( $v_p$ ) and shear ( $v_s$ ) sound velocities was carried out using Eq. 3:

$$v = \frac{\Delta\omega\lambda}{2 \sin(\theta/2)} \quad (3)$$

where  $\lambda$  is the laser wavelength and  $\theta$  is the angle between the incident and scattered beams<sup>92,93</sup>. We collected 8 spectra for each sample at different rotation angles (from  $-180^\circ$  to  $+180^\circ$ ) to factor for uncertainties. Finally, we calculated the  $K/G$  factor using the ratio between  $v_p$  and  $v_s$  (Eq. 4):

$$\frac{K}{G} = \left(\frac{v_p}{v_s}\right)^2 - \frac{4}{3} \quad (4)$$

### Room- and high-temperature Raman spectroscopy

Glasses subjected to micropenetration, concentric cylinder viscometry, C-DSC and F-DSC were analysed before and after the measurements to account for potential modifications (i.e., crystallization and/or iron oxidation). For this, we used a confocal Raman imaging microscope at the Institute of Non-Metallic Materials, TU Clausthal (alpha300R, WITec GmbH), where spectra were acquired using a 100x objective in the ranges between 10 and 1300 cm<sup>-1</sup>. Acquisition parameters included an integration time of 10 s, an accumulation count of 5, and a laser power of 10 mW. Spectra were smoothed to enhance the signal-to-noise ratio.

Additionally, we performed in situ high-temperature Raman analyses on the AND100 sample. We targeted the same temperatures and heating treatments as those used for micropenetration experiments. We used a Renishaw InVia Qontor Raman spectrometer at the CEMHTI, Orleans (France). Spectra were acquired using a 20x NA 0.35 objective in the ranges between 150 and 2000 cm<sup>-1</sup>. Acquisition parameters included an integration time of 60 seconds, and a laser power of 20 mW.

### Mössbauer spectroscopy

Mössbauer measurements were performed at the Bayerisches Geoinstitut (University of Bayreuth, Germany). Glass samples of ~4 mm diameter and ~600 μm thickness were measured before and after experiments at room temperature (293 K) using a constant acceleration Mössbauer spectrometer equipped with a high specific activity (370 MBq)<sup>57</sup>Co point source within a 12 μm thick Rh matrix. Calibration of the velocity scale was relative to a 25 μm thick α-Fe foil, and data were gathered within the range of  $\pm 5 \text{ mm s}^{-1}$ , with acquisition durations of 2 to 3 days each. The recorded spectra were fitted with the full transmission integral using the MossA software<sup>94</sup>. Finally, the resulting Fe<sup>3+</sup>/Fe<sup>2+</sup> ratios were calculated using the relative area associated with each iron species.

### Room- and high-temperature transmission electron microscopy (TEM) analyses

We performed room-temperature scanning TEM (STEM) analyses on the AND100 samples post-micropenetration experiments and in situ heating TEM observations on the AND100 starting glass. Room-temperature STEM explorations were performed at the Bayerisches Geoinstitut (University of Bayreuth, Germany) using a FEI Titan G2 80-200S/TEM. STEM imaging was acquired from lamellas made using a focused ion beam (FIB) with thicknesses ranging from 24(2) to 50(2) nm. These lamellas were extracted from the same samples that were used for micropenetration experiments, utilizing a SCIOS Dual Beam system from FEI Company. We used a Gallium ion beam with variable current, from 7.8 pA to 300 nA depending on the precision requirements. Analytical scanning transmission electron microscopy (STEM) micrographs were collected at 200 kV using an energy-dispersive X-ray spectrometer (EDS) system consisting of four silicon drift detectors (Bruker, QUANTAX EDS). The EDS maps were acquired with a dwell time of 16 s using a sub-nanometer-sized electron beam with less than 0.05 nA probe current at 200 kV-acceleration voltage.

To accumulate statistically relevant characteristic X-ray counts in a quantitative EDS map, the total acquisition time was 12–30 minutes. During the acquisition, an image drift correction function was always activated to prevent drift in the profile. To get quantitative compositions of the samples, we corrected the Z-number and absorption effects on the evaluations of the EDS spectrum<sup>95,96</sup>. Geometrical analyses of STEM-HAADF images were subjected to pixel segmentation and classification using the ilastik software, version 1.4.0<sup>97</sup>. To identify nanocrystalline phases in the silicate glasses, TEM-SAED patterns were collected after exploration in conventional TEM mode.

In situ heating experiments were performed at the CNRS CEMHTI in Orléans (France) using a JEOL ARM200F (JEOL Ltd.) Cold FEG microscope operating at 80 kV, mounting a double spherical aberration corrector, a Gatan Imaging Filter (GIF, Gatan Ltd.) and a OneView camera. The experimental procedure was optimized in a previous work<sup>45</sup> to minimize artifacts and sample damage due to highly energetic electron irradiation. The AND100 glass was crushed and ground in an agate mortar, adding ethanol to obtain a diluted suspension; one drop of the liquid was then loaded onto a MEMS grid specifically adapted for a Protochips Fusion double-tilt heating holder and dried in air overnight. Plasma cleaning was avoided to prevent major changes in the redox state of iron in the sample. After introducing the sample holder into the TEM column, it was pre-emptively treated at 200 °C for 1 h to remove possible volatile contaminants. The subsequent in situ experiment involved manual heating at 1 °C s<sup>-1</sup> to various temperatures between 200 °C and 750 °C, where isothermal dwells of 30–60 s were applied to facilitate nanoscale observation in TEM mode (Supplementary Fig. 6). Sample drift was manually compensated during the heating ramps. After the experiment, the acquired data was manually resampled (3 images for each isothermal dwell) and re-aligned using the software DigitalMicrograph GMS.3 (Gatan). To identify nanocrystalline phases in the silicate glasses, we performed Fast Fourier transform (FFT) on HR-TEM images. The EDS maps were taken in STEM mode with an acquisition time of 30 s using a sub-nanometer-sized electron beam of 1 Å. To accumulate statistically relevant characteristic X-ray counts in a quantitative EDS map, the total acquisition time was approximately 11 min.

### Viscosity parametrization

The combination of C-DSC, F-DSC, MP and CC viscosity data enabled the parametrization of the melt viscosity of our samples as a function of temperature  $\eta(T)$ , via the Mauro–Yue–Ellison–Gupta–Allan (MYEGA) equation (Eq. 5)<sup>54</sup>:

$$\log_{10}\eta(T) = \log_{10}\eta_{\infty} + (12 - \log_{10}\eta_{\infty}) \frac{T_g}{T} \exp\left[\left(\frac{m}{12 - \log_{10}\eta_{\infty}} - 1\right) \left(\frac{T_g}{T} - 1\right)\right] \quad (5)$$

where  $\log_{10}\eta_{\infty} = -2.93 \pm 0.3$  is the logarithmic viscosity at infinite temperature<sup>53,54</sup>,  $T_g$  is the glass transition temperature (in K) determined by C-DSC ( $T_{onset}$  at  $q_{h,c} = 10$  °C min<sup>-1</sup>) and  $m$  is the melt fragility defined in Eq. 6<sup>98</sup> as the slope of viscosity curve evaluated at  $T_g$ :

$$m = \left. \frac{\partial \log_{10}\eta}{\partial T_g/T} \right|_{T=T_g} \quad (6)$$

The melt fragility parameter,  $m$ , can be determined by fitting Eq. 5 to our viscosity datasets (Supplementary Table 2) and the measured  $T_g$  via C-DSC (Table 1). Additionally,  $m$  also can be inferred from BLS measurements using the empirical relationship introduced by Cassetta et al.<sup>99</sup> (Eq. 7),

$$m = 43 \cdot \frac{K}{G} - 31 \quad (7)$$

### Small- and -wide angle X-ray scattering (SAXS and WAXS)

The SAXS and WAXS measurements were conducted at the ID02 beamline of the European Synchrotron Radiation Facility (ESRF)<sup>67</sup> in Grenoble, France. The experiments utilized a monochromatic, highly collimated, and intense X-ray beam in a pinhole configuration, with a sample-to-detector distance of 6 meters. This arrangement enabled the exploration of a scattering vector range from 0.01 nm<sup>-1</sup> to 2.5 nm<sup>-1</sup>, where  $q$  is the scattering vector, defined as

$$q = |q| = \frac{4\pi \sin(\theta)}{\lambda}, \quad (8)$$

with the X-ray wavelength  $\lambda = 1$  Å and  $\theta$  is the scattering angle. To eliminate parasitic background around the primary beam, a guard slit before the sample was set to 0.45 mm vertically and 0.5 mm horizontally. Data reduction was performed using PyFAI, which leverages the geometry of ID02.

The analysis of the SAXS data was performed using a custom-developed software package, which has been successfully validated and applied in previous studies<sup>100,101</sup>. Assuming a spherical form factor for the nanoparticles, and based on TEM observations indicating potential close contact among the nanoparticles, the scattering intensity,  $I(q)$ , was modeled using the decoupling approximation<sup>100,102–104</sup>:

$$I(q) = \Delta(\rho)^2 S(q) P(q) + bck + \frac{K_{Porod}}{q^4} \quad (9)$$

where  $\Delta(\rho)^2$  is the difference of electronic density between the nanoparticles and the surroundings,  $bck$  is the background constant,  $P(q)$  is the contribution given by a poly-disperse system of not-interacting homogeneous spheres,

$$P(q) = \int_a^{\infty} D(\bar{R}, r) F(r, q, \bar{R})^2 r^6 dr \quad (10)$$

$F(q, r)$  is the form factor of a sphere of radius  $r$  given by Eq. 11

$$F(q, r) = \frac{\sin(qr) - qr \cos(qr)}{qr^3} \quad (11)$$

and  $D(r, \bar{R})$  is the Weibull size distribution of particle sizes defined as

$$D(r, \bar{R}) = \left(\frac{r}{\bar{R}}\right)^{(b-1)} \exp\left(-\frac{r}{\bar{R}}\right)^b, \quad (12)$$

in which  $\bar{R}$  is the average radius of the nanoparticle. The possibility of having a bimodal distribution is also included in the fitting. In this case the distribution function is given by the sum of two Weibull distribution functions centered in  $R_1$  and  $R_2$ .  $S(q)$  is the structure factor for interacting spheres with a hard-sphere radius  $R_{HS}$ , constituting the effective interaction distance between particles. The  $\eta_{HS}$  is the hard sphere volume fraction.  $S(q)$  can be calculated analytically using the PercusYevick approximation which works well for systems characterized by a short-range interaction potential. Accordingly,  $S(q)$  is equal to:

$$S(q, R_{HS}) = [1 + 24\eta_{HS}f(R_{HS}, q)]^{-1} \quad (13)$$

and by defining  $x = R_{HS} q$  it is possible to arrange  $f(x)$  as the following:

$$f(x) = \frac{\alpha(-x \cos x + \sin x)}{x^3} + \frac{\beta(-x^2 \cos x + 2x \sin x + 2 \cos x - 2)}{x^4} + \frac{\gamma[-x^4 \cos x + 4x^3 \sin x + 12x^2 \cos x - 24x \sin x - 24 \cos x + 24]}{x^5} \quad (14)$$

with,

$$\alpha = \frac{(1 + 2\eta_{HS})^2}{(1 - \eta_{HS})^4}, \quad (15)$$

$$\beta = \frac{-6\eta_{HS}(1 + \frac{\eta_{HS}}{2})^2}{(1 - \eta_{HS})^4} \quad (16)$$

$$\gamma = \frac{\eta_{HS}\alpha}{2} \quad (17)$$

Finally, by assuming that a particle grows at the expense of the surrounding iron oxide content,  $R_{HS}$  is proportional to the actual nanoparticle radius  $R_{HS} = 2Rkc^{100,102,103}$ , where  $kc$  is a constant term  $\geq 1$ . This parameter considers the possibility that the nanoparticles are not fully in contact. To reproduce the SAXS pattern at very low  $q$  a Porod behavior  $K_{porod}/q^4$  has also been added. This inverse fourth power dependence indicates that at high  $q$  values, the scattering intensity decreases sharply. The Porod function is instrumental in understanding the surface roughness and the specific surface area of the particles in the sample. It assumes an ideal, smooth interface, leading to a clean power law, but deviations from this behavior can reveal information about surface fractal dimensions and the nature of the interface.

Finally, we calculated  $d$ -spacings ( $d$ ) for the crystalline phases from WAXS experiments using Eq. 18<sup>105</sup>,

$$d = \frac{2\pi}{q_{peak}} \quad (18)$$

with  $q_{peak}$  corresponding to the WAXS peaks (Fig. 6b).

### Data availability

Data supporting the findings of this study are available within the article or in the Supplementary Information. Additional source data for figures are available in the following link: <https://zenodo.org/records/15342490>.

Received: 2 October 2024; Accepted: 28 May 2025;

Published online: 12 June 2025

### References

- Loughlin, S. C., Sparks, S., Brown, S. K., Jenkins, S. F. & Vye-Brown, C. *Global Volcanic Hazards and Risk. Global Volcanic Hazards and Risk* (Cambridge University Press, Cambridge, 2015). <https://doi.org/10.1017/CBO97811316276273>.
- Papale, P. Strain-induced magma fragmentation in explosive eruptions. *Nature* **397**, 425–428 (1999).
- Gonnermann, H. M. Magma Fragmentation. *Annu. Rev. Earth Planet. Sci.* **43**, 431–458 (2015).
- Cashman, K. V. & Scheu, B. *Magmatic Fragmentation. The Encyclopedia of Volcanoes*. <https://doi.org/10.1016/b978-0-12-385938-9.00025-0> (Elsevier Inc., 2015).
- Cassidy, M., Manga, M., Cashman, K. & Bachmann, O. Controls on explosive-effusive volcanic eruption styles. *Nat. Commun.* **9**, 2839 (2018).
- Kueppers, U., Scheu, B., Spieler, O. & Dingwell, D. B. Fragmentation efficiency of explosive volcanic eruptions: A study of experimentally generated pyroclasts. *J. Volcanol. Geotherm. Res.* **153**, 125–135 (2006).
- Mueller, S., Scheu, B., Spieler, O. & Dingwell, D. B. Permeability control on magma fragmentation. *Geology* **36**, 399–402 (2008).
- Dingwell, D. B. Volcanic dilemma: Flow or blow?. *Science* **273**, 1054–1055 (1996).
- Okumura, S., Nakamura, M., Nakano, T., Uesugi, K. & Tsuchiyama, A. Shear deformation experiments on vesicular rhyolite: implications for brittle fracturing, degassing, and compaction of magmas in volcanic conduits. *J. Geophys. Res. Solid Earth* **115**, 1–10 (2010).
- Arzilli, F. et al. Magma fragmentation in highly explosive basaltic eruptions induced by rapid crystallization. *Nat. Geosci.* **12**, 1023–1028 (2019).
- La Spina, G., Burton, M., De’Michieli Vitturi, M. & Arzilli, F. Role of syn-eruptive plagioclase disequilibrium crystallization in basaltic magma ascent dynamics. *Nat. Commun.* **7**, (2016).
- La Spina, G. et al. Explosivity of basaltic lava fountains is controlled by magma rheology, ascent rate and outgassing. *Earth Planet. Sci. Lett.* **553**, 116658 (2020).
- Bamber, E. C. et al. Outgassing behaviour during highly explosive basaltic eruptions. *Commun. Earth Environ.* **5** (2024).
- Sato, H. et al. Viscosity of andesitic lava and its implications for possible drain-back processes in the 2011 eruption of the Shinmoedake volcano, Japan. *Earth, Planets Sp.* **65**, 623–631 (2013).
- Vetere, F., Iezzi, G., Perugini, D. & Holtz, F. Rheological changes in melts and magmas induced by crystallization and strain rate. *Comptes Rendus. Géoscience* **354**, 227–248 (2022).
- Yamada, K., Emori, H. & Nakazawa, K. Time-evolution of bubble formation in a viscous liquid. *Earth, Planets Sp.* **60**, 661–679 (2008).
- Bamber, E. C. et al. Pre- and syn-eruptive conditions of a basaltic Plinian eruption at Masaya Volcano, Nicaragua: The Masaya Triple Layer (2.1 ka). *J. Volcanol. Geotherm. Res.* **392**, 106761 (2020).
- Sable, J. E., Houghton, B. F., Del Carlo, P. & Coltelli, M. Changing conditions of magma ascent and fragmentation during the Etna 122 BC basaltic Plinian eruption: Evidence from clast microtextures. *J. Volcanol. Geotherm. Res.* **158**, 333–354 (2006).
- Okumura, S. et al. Rheology of nanocrystal-bearing andesite magma and its roles in explosive volcanism. *Commun. Earth Environ.* **3**, 241 (2022).
- Valdivia, P. et al. Are volcanic melts less viscous than we thought? The case of Stromboli basalt. *Contrib. to Mineral. Petrol.* **178**, 45 (2023).
- Scarani, A. et al. A chemical threshold controls nanocrystallization and degassing behaviour in basalt magmas. *Commun. Earth Environ.* **3**, 284 (2022).
- Liebske, C., Behrens, H., Holtz, F. & Lange, R. A. The influence of pressure and composition on the viscosity of andesitic melts. *Geochim. Cosmochim. Acta* **67**, 473–485 (2003).
- Fanesi, E. et al. A review of the differential scanning calorimetry shift-factor approach: Application to Colli Albani melt viscosity and implications for mafic Plinian eruptions. *J. Volcanol. Geotherm. Res.* **461**, 108276 (2025).
- Zellmer, G. F. et al. Inferring the effects of compositional boundary layers on crystal nucleation, growth textures, and mineral chemistry in natural volcanic tephra through submicron-resolution imaging. *Front. Earth Sci.* **4**, 1–7 (2016).
- Di Genova, D. et al. A compositional tipping point governing the mobilization and eruption style of rhyolitic magma. *Nature* **552**, 235–238 (2017).
- Eichheimer, P. et al. Combined numerical and experimental study of microstructure and permeability in porous granular media. *Solid Earth Discuss.* 1–25 <https://doi.org/10.5194/se-2019-199> (2020).
- Knafelc, J. et al. Havre 2012 pink pumice is evidence of a short-lived, deep-sea, magnetite nanolite-driven explosive eruption. *Commun. Earth Environ.* **3**, 1–11 (2022).
- Barone, G. et al. Nanoscale surface modification of Mt. Etna volcanic ashes. *Geochim. Cosmochim. Acta* **174**, 70–84 (2016).
- Mujin, M. & Nakamura, M. A nanolite record of eruption style transition. *Geology* **42**, 611–614 (2014).
- Yoshida, K. et al. Oxidation-induced nanolite crystallization triggered the 2021 eruption of Fukutoku-Oka-no-Ba. *Japan. Sci. Rep.* **13**, 7117 (2023).
- Sharp, T. G., Stevenson, R. J. & Dingwell, D. B. Microlites and ‘nanolites’ in rhyolitic glass: Microstructural and chemical characterization. *Bull. Volcanol.* **57**, 631–640 (1996).
- Mujin, M. & Nakamura, M. Late-stage groundmass differentiation as a record of magma stagnation, fragmentation, and rewelding. *Bull. Volcanol.* **82** (2020).

33. Cáceres, F. et al. Oxide nanolitisation-induced melt iron extraction causes viscosity jumps and enhanced explosivity in silicic magma. *Nat. Commun.* **15** (2024).
34. Pereira, L. et al. The rheological response of magma to nanolitisation. *J. Volcanol. Geotherm. Res.* **448**, 108039 (2024).
35. Di Genova, D. et al. In situ observation of nanolite growth in volcanic melt: A driving force for explosive eruptions. *Sci. Adv.* **6**, (2020).
36. Cáceres, F. et al. Can nanolites enhance eruption explosivity?. *Geology* **48**, 997–1001 (2020).
37. Mujin, M., Nakamura, M. & Miyake, A. Eruption style and crystal size distributions: Crystallization of groundmass nanolites in the 2011 Shinmoedake eruption. *Am. Mineral.* **102**, 2367–2380 (2017).
38. Di Genova, D., Caracciolo, A. & Kolzenburg, S. Measuring the degree of “nanolitization” of volcanic glasses: Understanding syn-eruptive processes recorded in melt inclusions. *Lithos* **318–319**, 209–218 (2018).
39. Giordano, D., Russell, J. K. & Dingwell, D. B. Viscosity of magmatic liquids: A model. *Earth Planet. Sci. Lett.* **271**, 123–134 (2008).
40. Di Genova, D., Zandonà, A. & Deubener, J. Unravelling the effect of nano-heterogeneity on the viscosity of silicate melts: Implications for glass manufacturing and volcanic eruptions. *J. Non. Cryst. Solids* **545**, 120248 (2020).
41. Bondar, D. et al. Nanolite Crystallization in Volcanic Glasses: Insights From High-Temperature Raman Spectroscopy and Low-Temperature Rock-Magnetic Analysis. *Geochemistry, Geophys. Geosystems* **26** (2025).
42. Stabile, P. et al. The effect of iron and alkali on the nanocrystal-free viscosity of volcanic melts: A combined Raman spectroscopy and DSC study. *Chem. Geol.* **559**, 119991 (2021).
43. Shebanova, O. N. & Lazor, P. Raman spectroscopic study of magnetite (FeFe<sub>2</sub>O<sub>4</sub>): a new assignment for the vibrational spectrum. *J. Solid State Chem.* **174**, 424–430 (2003).
44. Jubb, A. M. & Allen, H. C. Vibrational Spectroscopic Characterization of Hematite, Maghemite, and Magnetite Thin Films Produced by Vapor Deposition. *ACS Appl. Mater. Interfaces* **2**, 2804–2812 (2010).
45. Zandonà, A. et al. Crystallization Mechanism of Gel-Derived SiO<sub>2</sub>-TiO<sub>2</sub> Amorphous Nanobeads Elucidated by High-Temperature In Situ Experiments. *Cryst. Growth Des.* **23**, 4545–4555 (2023).
46. Deubener, J. et al. Updated definition of glass-ceramics. *J. Non. Cryst. Solids* **501**, 3–10 (2018).
47. Charles, R. J. Metastable Liquid Immiscibility in Alkali Metal Oxide–Silica Systems. *J. Am. Ceram. Soc.* **49**, 55–62 (1966).
48. Wechsler, B. A., Lindsley, D. H. & Prewitt, C. T. Crystal structure and cation distribution in titanomagnetites (Fe<sub>3-x</sub>Ti<sub>x</sub>O<sub>4</sub>). *Am. Mineral.* **69**, 754–770 (1984).
49. Zinin, P. et al. Raman spectroscopy of titanomagnetites: Calibration of the intensity of Raman peaks as a sensitive indicator for their Ti content. *Am. Mineral.* **96**, 1537–1546 (2011).
50. Cormier, L., Galoisy, L., Lelong, G. & Calas, G. From nanoscale heterogeneities to nanolites: cation clustering in glasses. *Comptes Rendus. Phys.* **24**, 199–214 (2024).
51. Thivet, S. et al. Metastable liquid immiscibility in the 2018–2021 Fani Maoré lavas as a mechanism for volcanic nanolite formation. *Commun. Earth Environ.* **4** (2023).
52. Zandonà, A. et al. Non-stoichiometric crystal nucleation in a spodumene glass containing TiO<sub>2</sub> as seed former: Effects on the viscosity of the residual melt. *J. Non. Cryst. Solids* **619**, 122563 (2023).
53. Langhammer, D., Di Genova, D. & Steinle-Neumann, G. Modeling the Viscosity of Anhydrous and Hydrated Volcanic Melts. *Geochemistry, Geophys. Geosystems* **22**, 1–26 (2021).
54. Mauro, J. C., Yue, Y., Ellison, A. J., Gupta, P. K. & Allan, D. C. Viscosity of glass-forming liquids. *Proc. Natl. Acad. Sci. USA.* **106**, 19780–19784 (2009).
55. Araya, N. et al. Shallow magma pre-charge during repeated Plinian eruptions at Sakurajima volcano. *Sci. Rep.* **9**, 1–10 (2019).
56. Scherrer, M. C., Hess, K., Fehr, K. T. & Dingwell, D. B. Oxidation-state dependence of rheology in peralkaline glasses of phonolitic composition. *Geophys. Res. Abstr.* **14**, 5805 (2012).
57. Dingwell, D. B. Redox viscometry of some Fe-bearing silicate melts. *Am. Mineral.* **76**, 1560–1562 (1991).
58. Okumura, S. et al. Rheology of nanocrystal-bearing andesite magma and its roles in explosive volcanism. *Commun. Earth Environ.* **3**, 1–7 (2022).
59. Singh, M. et al. Vapour phase approach for iron oxide nanoparticle synthesis from solid precursors. *J. Solid State Chem.* **200**, 150–156 (2013).
60. Koch, A. Neue Minerale aus dem Andesit des Aranyer Berges in Siebenbürgen. *Mineral. und Petrogr. Mitteilungen* **1**, 331–361 (1878).
61. Muthukumar, K. et al. Synthesis and characterization of magnetic copper-iron-titanate and uptake studies of americium from nuclear waste solutions. *RSC Adv.* **6**, 111822–111830 (2016).
62. Guo, C. & Zhang, Y. Multicomponent diffusion in silicate melts: SiO<sub>2</sub>-TiO<sub>2</sub>-Al<sub>2</sub>O<sub>3</sub>-MgO-CaO-Na<sub>2</sub>O-K<sub>2</sub>O System. *Geochim. Cosmochim. Acta* **195**, 126–141 (2016).
63. Honour, V. C. et al. Compositional boundary layers trigger liquid unmixing in a basaltic crystal mush. *Nat. Commun.* **10** (2019).
64. Kleebusch, E., Patzig, C., Höche, T. & Rüssel, C. The evidence of phase separation droplets in the crystallization process of a Li<sub>2</sub>O-Al<sub>2</sub>O<sub>3</sub>-SiO<sub>2</sub> glass with TiO<sub>2</sub> as nucleating agent – An X-ray diffraction and (S)TEM-study supported by EDX-analysis. *Ceram. Int.* **44**, 2919–2926 (2018).
65. Raghuwanshi, V. S., Harizanova, R., Tatchev, D., Hoell, A. & Rüssel, C. Structural analysis of Fe-Mn-O nanoparticles in glass ceramics by small angle scattering. *J. Solid State Chem.* **222**, 103–110 (2015).
66. Fielitz, P., Hensch, G., Borchardt, G. & Deubener, J. Al-26 and O-18 tracer diffusion in a titania-coated sodium aluminosilicate glass. *J. Non. Cryst. Solids* **614**, 122400 (2023).
67. Narayanan, T. et al. Performance of the time-resolved ultra-small-angle X-ray scattering beamline with the Extremely Brilliant Source. *J. Appl. Crystallogr.* **55**, 98–111 (2022).
68. Cameron, M., Sueno, S., Prewitt, C. T. & Papike, J. J. High-Temperature crystal chemistry of acmite, diopside, hedenbergite, jadeite, spodumene, and Ureyite. *Am. Mineral.* **58**, 594–618 (1973).
69. Mader, H. M., Llewellyn, E. W. & Mueller, S. P. The rheology of two-phase magmas: A review and analysis. *J. Volcanol. Geotherm. Res.* **257**, 135–158 (2013).
70. Hess, P. C. Chapter 6. Thermodynamic Mixing Properties And The Structure Of Silicate Melts. in *Structure, Dynamics, and Properties of Silicate Melts* (eds. Stebbins, J. F., McMillan, P. F. & Dingwell, D. B.) 145–190. <https://doi.org/10.1515/9781501509384-008> (De Gruyter, Berlin, Boston, 1995).
71. Bouhifd, M. A., Richet, P., Besson, P., Roskosz, M. & Ingrin, J. Redox state, microstructure and viscosity of a partially crystallized basalt melt. *Earth Planet. Sci. Lett.* **218**, 31–44 (2004).
72. Chevrel, M. O., Giordano, D., Potuzak, M., Courtial, P. & Dingwell, D. B. Physical properties of CaAl<sub>2</sub>Si<sub>2</sub>O<sub>8</sub>-CaMgSi<sub>2</sub>O<sub>6</sub>-FeO-Fe<sub>2</sub>O<sub>3</sub> melts: Analogues for extra-terrestrial basalt. *Chem. Geol.* **346**, 93–105 (2013).
73. Tuheen, M. I., Wilkins, M. C., McCloy, J. & Du, J. The structures of iron silicate glasses with varying iron redox ratios from molecular dynamics simulations and EXAFS analysis. *J. Non. Cryst. Solids* **624**, 122713 (2024).
74. Di Genova, D. et al. In situ observation of nanolite growth in volcanic melt: A driving force for explosive eruptions. *Sci. Adv.* **6**, eabb0413 (2020).
75. Mollo, S. & Hammer, J. E. Dynamic crystallization in magmas. *Mineral reaction kinetics: Microstructures, textures, chemical and isotopic signatures* vol. 16 0 at <https://doi.org/10.1180/EMU-notes.16.12> (2017).

76. Di Fiore, F. et al. Magma titanium and iron contents dictate crystallization timescales and rheological behaviour in basaltic volcanic systems. *Commun. Earth Environ.* **5**, (2024).
77. Turner, M. B., Cronin, S. J., Bebbington, M. S., Smith, I. E. M. & Stewart, R. B. Relating magma composition to eruption variability at andesitic volcanoes: A case study from Mount Taranaki, New Zealand. *Bull. Geol. Soc. Am.* **123**, 2005–2015 (2011).
78. Dubosq, R. et al. Bubbles and atom clusters in rock melts: A chicken and egg problem. *J. Volcanol. Geotherm. Res.* **428**, (2022).
79. Kennedy, B. M., Jellinek, A. M., Russell, J. K., Nichols, A. R. L. & Vigouroux, N. Time- and temperature-dependent conduit wall porosity: A key control on degassing and explosivity at Tarawera volcano, New Zealand. *Earth Planet. Sci. Lett.* **299**, 126–137 (2010).
80. McBirney, A. R. Factors governing the intensity of explosive andesitic eruptions. *Bull. Volcanol.* **37**, 443–453 (1973).
81. Hornby, A. J. et al. Nanoscale silicate melt textures determine volcanic ash surface chemistry. 1–10 (2024).
82. Hughes, E. C. et al. Low analytical totals in EPMA of hydrous silicate glass due to sub-surface charging: obtaining accurate volatiles by difference. *Chem. Geol.* **505**, 48–56 (2019).
83. Behrens, H. et al. Structural relaxation mechanisms in hydrous sodium borosilicate glasses. *J. Non. Cryst. Solids* **497**, 30–39 (2018).
84. Di Genova, D., Romano, C., Alletti, M., Misiti, V. & Scarlato, P. The effect of CO<sub>2</sub> and H<sub>2</sub>O on Etna and Fondo Riccio (Phlegrean Fields) liquid viscosity, glass transition temperature and heat capacity. *Chem. Geol.* **377**, 72–86 (2014).
85. Douglas, R. W., Armstrong, W. L., Edward, J. & Hall, D. A penetration viscometer. *Glas. Technol.* **6**, 52–55 (1965).
86. Meerlender, G. Viskositäts-Temperaturverhalten des Standardglases I der DGG. *Glas. Ber.* **47**, 1–3 (1974).
87. Di Fiore, F. et al. Experimental insights on the shear-induced crystallization of a phonotephrite magma. *Chem. Geol.* **637**, 121682 (2023).
88. Di Fiore, F., Vona, A., Costa, A., Mollo, S. & Romano, C. Quantifying the influence of cooling and shear rate on the disequilibrium rheology of a trachybasaltic melt from Mt. Etna. *Earth Planet. Sci. Lett.* **594**, 117725 (2022).
89. Al-Mukadam, R., Di Genova, D., Bornhöft, H. & Deubener, J. High rate calorimetry derived viscosity of oxide melts prone to crystallization. *J. Non. Cryst. Solids* **536**, 119992 (2020).
90. Yue, Y. The iso-structural viscosity, configurational entropy and fragility of oxide liquids. *J. Non. Cryst. Solids* **355**, 737–744 (2009).
91. Zheng, Q., Mauro, J. C. & Yue, Y. Reconciling calorimetric and kinetic fragilities of glass-forming liquids. *J. Non. Cryst. Solids* **456**, 95–100 (2017).
92. Whitfield, C. H., Brody, E. M. & Bassett, W. Elastic moduli of NaCl by Brillouin scattering at high pressure in a diamond anvil cell. *Rev. Sci. Instrum.* **47**, 942–947 (1976).
93. Sinogeikin, S. et al. Brillouin spectrometer interfaced with synchrotron radiation for simultaneous x-ray density and acoustic velocity measurements. *Rev. Sci. Instrum.* **77** (2006).
94. Prescher, C., McCammon, C. & Dubrovinsky, L. MossA: a program for analyzing energy-domain Mössbauer spectra from conventional and synchrotron sources. *J. Appl. Crystallogr.* **45**, 329–331 (2012).
95. Van Cappellen, E. & Doukhan, J. C. Quantitative transmission X-ray microanalysis of ionic compounds. *Ultramicroscopy* **53**, 343–349 (1994).
96. Van Cappellen, E. The parameterless correction method in X-ray microanalysis. *Microsc. Microanal. Microstruct.* **1**, 1–22 (1990).
97. Berg, S. et al. Ilastik: interactive machine learning for (Bio)Image analysis. *Nat. Methods* **16**, 1226–1232 (2019).
98. Angell, C. A. Formation of glasses from liquids and biopolymers. *Science* **267**, 1924–1935 (1995).
99. Cassetta, M. et al. Estimating the viscosity of volcanic melts from the vibrational properties of their parental glasses. *Sci. Rep.* **11**, 1–14 (2021).
100. Longo, A. et al. Dynamic role of gold d-orbitals during CO oxidation under aerobic conditions. *ACS Catal.* **12**, 3615–3627 (2022).
101. Maurizio, C. et al. Grazing-incidence small-angle X-ray scattering and X-ray diffraction from magnetic clusters obtained by Co + Ni sequential ion implantation in silica. *J. Appl. Crystallogr.* **36**, 732–735 (2003).
102. Jensen, H. et al. Determination of size distributions in nanosized powders by TEM, XRD, and SAXS. *J. Exp. Nanosci.* **1**, 355–373 (2006).
103. Jeffries, C. M. et al. *Small-Angle X-Ray and Neutron Scattering. Nature Reviews Methods Primers* vol. 1 (Springer US, 2021).
104. Förster, S. et al. Scattering curves of ordered mesoscopic materials. *J. Phys. Chem. B* **109**, 1347–1360 (2005).
105. Gumedde, T. P., Luyt, A. S., Pérez-Camargo, R. A., Tercjak, A. & Müller, A. J. Morphology, nucleation, and isothermal crystallization kinetics of Poly(Butylene Succinate) mixed with a polycarbonate/MWCNT masterbatch. *Polymers (Basel)* **10**, 1–22 (2018).
106. Arzilli, F. et al. Characterization of nanocrystals in volcanic glass. <https://doi.org/10.1515/ESRF-ES-1734554218>.
107. Prata, G. S. et al. A new parameterization of volcanic ash complex refractive index based on NBO/T and SiO<sub>2</sub> content. *J. Geophys. Res. Atmos.* **124**, 1779–1797 (2019).

## Acknowledgements

Pedro Valdivia (P.V.) and Danilo Di Genova (D.D.G.) acknowledge the funding by Deutsche Forschungsgemeinschaft (DFG) project DI 2751/2–1. D.D.G. acknowledges the funding from the European Research Council (ERC) under the European Union’s Horizon 2020 research and innovation programme (NANOVOLC, ERC Consolidator Grant – No. 101044772). D.D.G. acknowledges funding by MUR-PRIN Project (CRYSTALIKIN, 2022L2APNR). This project has benefited from the expertise and facilities of the Platform MACLE-CVL, which has been co-funded by the European Union and the Centre-Val de Loire Region (FEDER). Joachim Deubener acknowledges DFG for financial support via the grant DE 598/33-1. The Scios FIB and the Titan G2 STEM at Bayerisches Geoinstitut were financed by DFG Grants INST 91/315-1 FUGG and INST 91/251–1 FUGG, respectively. Mathieu Allix and Cécile Genevois acknowledge funding from the Agence Nationale de la Recherche (ANR) through project ANR–23-CE08-0013-01. Claudia Romano and Alessandro Vona acknowledge funding by MUR-PRIN Project P20222BP7J. We acknowledge the European Synchrotron Radiation Facility (ESRF) for provision of synchrotron radiation facilities under proposal number ES-1474<sup>106</sup> and we would like to thank Peter Boesecke for assistance and support in using beamline ID02. We thank Alexander Rother and Raphael Njul for sample preparation, Dorothea Wiesner for the FIB lamella preparation and Catherine McCammon for facilitating the Mössbauer facilities at the Bayerisches Geoinstitut. We thank Adrian Hornby and all other reviewers for their constructive feedback and continuous contributions throughout the review process.

## Author contributions

Pedro Valdivia (P.V.) drafted the original manuscript, synthesized the starting materials, processed the experimental data, performed the data analyses, derived the viscosity models, conducted Mössbauer experiments and constructed the figures and tables. P.V., Alessio Zandonà (A.Z.) and Danilo Di Genova (D.D.G.) conceptualized the original idea. A.Z. and Cécile Genevois carried out the in situ high-temperature TEM experiments. Dmitry Bondar and Aurélien Canizarès performed the high-temperature Raman measurements. P.V., Jessica Löschmann and D.D.G. conducted micro-penetration, room-temperature Raman and calorimetry analyses. P.V. and Nobuyoshi Miyajima executed the room-temperature TEM. P.V. and Fabrizio Di Fiore carried out concentric cylinder measurements. P.V., Alexander Kurnosov and Tiziana Boffa Ballaran performed the Brillouin analyses. Joachim Deubener, Claudia Romano, Alessandro Vona and Mathieu Allix facilitated laboratory access and instrument availability. P.V., A.Z., Emily C. Bamber and D.D.G. revised the manuscript following peer review. D.D.G.

and Alessandro Longo processed SAXS/WAXS data. All co-authors provided feedback and contributed to the final version of the manuscript.

### Funding

Open Access funding enabled and organized by Projekt DEAL.

### Competing interests

The authors declare no competing interests.

### Additional information

**Supplementary information** The online version contains supplementary material available at <https://doi.org/10.1038/s43247-025-02424-9>.

**Correspondence** and requests for materials should be addressed to Pedro Valdivia.

**Peer review information** *Communications Earth & Environment* thanks Adrian Hornby and the other, anonymous, reviewer(s) for their contribution to the peer review of this work. Primary Handling Editor: Carolina Ortiz Guerrero. A peer review file is available.

**Reprints and permissions information** is available at <http://www.nature.com/reprints>

**Publisher's note** Springer Nature remains neutral with regard to jurisdictional claims in published maps and institutional affiliations.

**Open Access** This article is licensed under a Creative Commons Attribution 4.0 International License, which permits use, sharing, adaptation, distribution and reproduction in any medium or format, as long as you give appropriate credit to the original author(s) and the source, provide a link to the Creative Commons licence, and indicate if changes were made. The images or other third party material in this article are included in the article's Creative Commons licence, unless indicated otherwise in a credit line to the material. If material is not included in the article's Creative Commons licence and your intended use is not permitted by statutory regulation or exceeds the permitted use, you will need to obtain permission directly from the copyright holder. To view a copy of this licence, visit <http://creativecommons.org/licenses/by/4.0/>.

© The Author(s) 2025